POLITECNICO
MILANO 1863

IBSL: Liquid propellant kick stage rocket motor design

Pablo Arbelo Cabrera (10904636)

Rafael Bautista Linde (10784248)

Alessandro Michelazzi (10709804)

Gantas Morozovas (10951581)

Daniele Scarinci (10684473)

Gonzalo Zamora Caballero (10911317)

Lenn Chiapparo (10913795)

Team Work Activity of Space Propulsion

Abstract

There are many different designs of liquid rocket engines but each mission needs a specific design for it's purpose and needs a lot of research, design and analysis. This scientific paper provides a comprehensive overview and analysis of the development of a liquid propellant kick stage rocket motor for a satellite, with a focus on comparing a green (low toxic) option with a standard design based on hydrazine and nitrogen tetroxide. The propulsion system is a kick stage for a generic orbit transfer of a small satellite (250kg). The design of the combustion chamber, nozzle, injector and cooling system for all cases (toxic and green) will be discussed in different sections of the paper. After the design the results are compared as well as the effects of upscaling and downscaling the thrust level. A decision on what the best type of fuel is will not be made since a trade-off is required for this decision and no correct answer is available.

Nomenclature and acronyms

a Sonic speed

A_c Chamber section area

A_e Exit section area

A_{side} Lateral area of the engine

A_t Throat section area

C_f Fanning friction coefficient

c_{pg} Specific heat coefficient at constant pressure of the gas mixture

c_{plc} Specific heat coefficient at constant pressure of the cooling film liquid phase

c_{pvc} Specific heat coefficient at constant pressure of the cooling film vapor phase

c_T Thrust coefficient

c^* Characteristic velocity

D_c Chamber section diameter

D_e Exit section diameter

D_t Throat section diameter

f Friction coefficient between the flow phases

g_0 Gravity acceleration constant

G_c Film coolant mass flow rate per unit area

G_g Mass flow rate per unit area

I_s Specific impulse

$I_{s,2D}$ Specific impulse with 2D losses

I_{tot} Total impulse

I_V Volumetric impulse

H Cooling film enthalpy

h_g Convective heat transfer coefficient

k Pressure losses coefficient

L^* Characteristic length

L_c Chamber length

L_{conv} Convergent length

L_{div} Divergent length

L_{Rao} Rao nozzle divergent length

M Mach number

$\dot{m}$ Mass flow rate

$\dot{m}_{coolant}$ Mass flow rate for regenerative cooling

$\dot{m}_{film}$ Mass flow rate for film cooling

$\dot{m}_{FU}$ Fuel mass flow rate

$\dot{m}_{OX}$ Oxidizer mass flow rate

m_{dry} Spacecraft dry mass

m_{He} Helium mass

m_p Propellant mass

M_{mol} Molar mass

m_{tank} Propellant tank mass

$m_{tank,He}$ Helium tank mass

MMH Monomethyl hydrazine

N	Number of injectors	v_e	Exit velocity
NTO	Nitrogen tetroxide	V_{tank}	Propellant tank volume
OF	Oxidizer to fuel mass ratio	$V_{tank,He}$	Helium tank volume
p_a	Ambient pressure	α	Half-opening angle for the divergent
p_c	Chamber pressure	β	Half-opening angle for the convergent
p_e	Exit pressure		
$p_{press,in}$	Initial pressure of the helium tank	γ	Specific heat ratio
p_t	Propellant's tank pressure	Δv	Velocity delta
Pr	Prandtl number	ΔT	Temperature delta
Q	Heat	ϵ	Expansion ratio
$\dot{q}$	Heat power	η	Film coolant efficiency
Re	Reynolds number	λ	Pressure losses coefficient for distributed losses
r_{curv}	Curvature radius	λ_{2D}	2D losses coefficient
T	Thrust	μ	Dinamic viscosity
T_{2D}	Thrust with 2D losses	σ	Correction factor for property variations across the boundary layer
T_c	Chamber temperature		
T_{aw}	Adiabatic wall temperature	θ_i	Initial parabola angle for the Bell nozzle
T_s	Storage temperature		
T_w	Wall temperature	θ_{inj}	Injection angle
V_c	Chamber volume	θ_e	Final parabola angle for the Bell nozzle

Contents

List of Figures

List of Tables

Chapter 1

Introduction

The company has been assigned the development of a liquid bi-propellant kick stage motor for a satellite. The propellant is required to be storable, whereas the choices of the propellant couple and engine size are some of the topics discussed in this dossier.

The propulsion system to be implemented is a kick stage, used to accomplish a generic orbit transfer of a small satellite. This rocket must grant a total Δv=2500m s^{-1} with a mass budget related to the dry mass of 250kg. While submitting to the aforementioned requirements regarding the engine, a trade-off comparison among standard hydrazine/nitrogen tetroxide propellant couple and a green alternative one will be conducted. This comparison is influenced by the ongoing movement in the space industry towards environmentally-friendly solutions. Furthermore, an engine upscaling and downscaling design will be carried out in order to prove the convenience of either the nominal size or the scaling modifications.

The study will include an initial short literature survey on topics such as kick stages, green propellants, metal compatibility and additive manufacturing. This would settle the grounds for the design process that will eventually lead to the proper engine architecture.

1.1   Nominal requirements

As touched upon in the previous paragraph, the liquid propellant system needs to meet several requirements with respect to both the mission outline and the technical requests. These requirements are the following:

- Total ΔV budget of 2500m s^{-1} with $m_{dry} = 250$kg.

- Constant thrust profile with no throttling.

- Not-self-pressurized propellant with standard pressure-fed (regulated) system.

- Propellant couple choice between toxic propellant (hydrazine/nitrogen tetroxide) and non-toxic propellant (hydrogen peroxide 98% + fuel subject to election).

- Injection plate design with either like-on-like or unlike injectors.

- Heat exchange solution that ensures a suitable cooling strategy.

- Compatibility of materials with the propellants and with additive manufacturing techniques.

Chapter 2

Design baseline selection

This chapter will focus on the different engineering choices and technological options that are available in the space industry until today in order to narrow down and refine the liquid bi-propellant engine baseline design.

2.1 Background on kick stages

A kick stage, also known as apogee kick motor (AKM), is a rocket motor that is regularly employed on artificial satellites to provide the final impulse to change the trajectory from the transfer orbit into its final one [1]. For instance, it is an extra stage that can be used in order to perform the circularization of orbits of small satellites.

One example is the Kick stage of the Electron launcher, developed by Rocket Lab ([2]). This last stage is going to be taken as a reference example for the general design of this project since it is characterised by similar performances and assigned requirements compared to the study case of this report. In a usual Electron mission, after the second stage has taken the payload to an elliptical orbit, the kick stage separates and begins a coast phase while carrying its small satellite payload. Once reaching apogee, its engine ignites. By doing so, it raises the perigee until the kick stage is orbiting around the Earth in a circle orbit ([2]).

By looking at the kick stage specifications in the *Electron Payload User's guide* ([3]), it can be concluded that the engine used is a *Curie* engine (characterisde by $40\,kg$ of dry mass), which uses a liquid bi-propellant in order to provide a thrust of $120\,N$. Limited data about an actual mission can be found in literature. However, in the Lunar Photon mission to the moon ([4]), Rocket Lab was selected as launch service provider for the NASA's CAPSTONE mission. In this case, the kick stage has a ΔV of more than $3000\,m/s$ using a HyperCurie engine (Hypergolic bi-propellant) with $480\,N$ of thrust and a vacuum specific impulse of $310\,s$. The expansion ratio of the nozzle is $\epsilon = 200$ and it is going to be taken as reference value for this study. The value is consistent since the normal range for these type upper stages is 150-300.

ESA targets Ariane 6 rocket missions using the *Astris* quick stage ([5]). Concretely, Astris will augment Ariane 6's ability to deploy multiple payloads into separate low Earth orbits on a single launch. It uses the *Berta* engine ([6]), a green rocket engine which, according to hot-fire tests, has a reference thrust of $2.5\,kN$ and it is built using an additive

layer manufacturing. However, there is no in depth information regarding this European engine. As confirmed in *Rocket Propulsion Elements* by G. P. Sutton [7], these values of thrust in this kind of propulsion system is typical and acceptable.

Moreover, the chamber pressure for this engine will be within $0.14 - 2.1\,MPa$. Similar thrust level designs have a comparable chamber pressure. For instance, *R-4D* small hypergolic rocket engine ($490\,N$) has a chamber pressure of $6.93\,N$. In addition, reference [8] shows the design of a motor with the desired non-toxic propellant and a similar thrust level requirement making use of a chamber pressure of 11.7 bar. Therefore, chamber pressure can be fixed to a reasonable value of $10\,bar$.

The most popular propellant mixture for small liquid-fuel thrusters is monomethylhydrazine (MMH, CH_6N_2) and nitrogen tetroxide (N_2O_4). The Orbital Maneuvering System, which was used on the Space Shuttle, and Tangential Injection and Rotational Combustion, used on the majority of the USA's classified satellites, are some of the upper stages rocket engines that utilise N_2O_4/MMH. The typical thrust generated by satellite propulsion systems is in the range of 400-900 N.[9]

The reason for the usage of the N_2O_4/MMH couple for upper stages is due to its high specific impulse, hypergolic nature, and exceptional storage stability. Its hypergolic characteristics allow to use this propellant couple in spaceship applications without the requirement for an external igniting device. NTO and MMH's primary flaw is their toxicity.

2.2 Green propellant alternatives

The considerable hazards given by the toxicity of some of the propellants used until today in the space industry (e.g. the N_2O_4/MMH couple) is the cause for the widespread interest towards green alternatives. Substances like hydrogen peroxide and nitrous oxide as oxidizers and light hydrocarbons, alcohols and kerosene as fuels not only have lower toxicity but also reduce the costs associated to suspension of activities, personal protection equipment, medical health, exhaustive surveillance, etc. [12].

When it comes to oxidizers, hydrogen peroxide is a non-toxic oxidizer with much less vapour hazard ratio than nitrous oxide. Moreover, 98% high test peroxide or HTP is a high density chemical ($1437 kg/m^3$ at 20 degrees) compliant with the normal boiling requirements (stated as flammability requirements) whereas it does not fulfil the freezing point limit (liquid range for handling and storage), except for low concentrations. Furthermore, there are several drawbacks such as its instability (unsuitable for long-term missions) and its incompatibilities regarding other materials, making it compatible just with a narrow set (aluminum 1060, fully austenitic stainless, teflon and polyethylene) [12].

Regarding "green" fuels, a choice has to be made between hydrocarbon, alcohols or kerosene. In order to select the propellant couple and its oxidizer-fuel ratio design point, the operational requirements of the mission have to be considered and a trade-off analysis between performances, temperature and subsystem has to be carried out.

Globally Harmonized System of Classification and Labelling of Chemicals (GHS, [13]) broadly indicates that the aforementioned substances are not toxic, even though each one

of them could present different risks for health ([12]). However, the exposure hazards of alcohols and kerosene is low, which increases the reason for their use for safe and green applications.

Several properties and performance results can be compared and distinguished between these different fuels. Hydrocarbons (high vapor pressure at 20 ℃) in combination with nitrous oxide may be advantageous on a self-pressurisation system (not suitable for the study case) whereas for alcohols and kerosene (liquids at normal atmospheric conditions) an external gas is employed ([12]).

Table 2.1: Propellant properties at 298K

Propellants

	Density $[kg/m^3]$	Viscosity $[Pa*s]$
MMH	874	$7.75*10^{-4}$
NTO	1448	$4.38*10^{-4}$
H2O2	1430	$1.1*10^{-3}$
RP-1	801	$1.595*10^{-3}$

Even though alcohols and kerosene are characterised by a lower energy density than hydrocarbon fuels, they allow a decrease in volume, especially notorious in the case of kerosene fuel when using the stated hydrogen peroxide (98%). In the report extracted from the literature ([12]), it is stated that the O/F which maximises the specific impulse is greater in the case of hydrocarbon, thus reducing the amount of fuel for cooling purposes. Finally, it is true that I_s in vacuum is flatter than in this latter case, which allows to slightly reduce the flame temperature when maximising this parameter (see figure 5 (a) in [12]).

Once having analysed all these different aspects, the fuel considered to be the most suitable is the kerosene. Not only does it allow to maximise the specific impulse, obtaining values close to the ones provided by the toxic propellant (Figure 2.1), but it also makes use of a low O/F ratio, which means more fuel for the cooling, and the flame temperature is not too elevate. Moreover, combined with the proposed oxidiser, it enables a major volume saving (Figure 2.2).
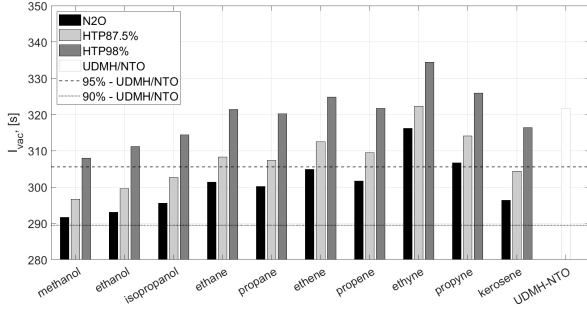
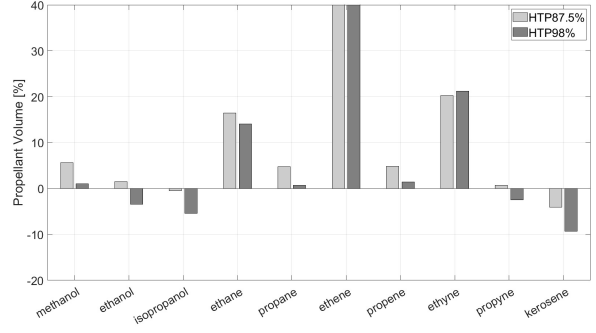Figure 2.1: Performance comparison with respect to UDMH/NTO system .

Figure 2.2: Relative volume with respect to UDMH/NTO system for a generic upper stage mission ($\Delta V = 3000 m/s$).

2.3 Metallic additive manufacturing

Any project, no matter its scale, not only has to look well on paper but also be possible to manufacture. In the 20th century engineers employed many workarounds while using traditional or Subtractive Manufacturing (SM) to get the most out of the technology of their time ([26]). Now, in the 21st century, a new frontier has opened. With the ability to compute more complex models for material heat deflection and a large growth in the private(desktop) 3D printing market, Additive Manufacturing (AM) is quickly becoming a main stay tool in the arsenal of engineers ([27]).

While working with SM, no matter the machine, there will be very serious limitations: complex paths/holes in the parts are not possible to create or require multi-part assemblies, a substantial amount of starting material used becomes waste, additional geometry comes at an exponential cost ([29]). When looked at these points in an environment with low production volumes and a significance on maximum performance, SM starts to lose appeal. AM has a much stronger basis in use for space and aerospace environments for research and development, small-scale production due to a per part cost that stays constant no matter the production quantity or complexity of the part ([29]).

AM can be divided into many categories by both material used and the way it builds up its parts. This review will focus mainly on the machines needed to produce rocket engine assemblies.

Firstly, using metal AM one may look at the granted design freedom. Usually an engine's combustion chamber (c.c) would be split into an assembly line that takes time to properly set up. If the required assembly's size and precision is compatible with a branch of metal AM, then the combustion chamber will not only be completed as a singular part but it will also incorporate the very complex injector plate into one part. This drastically speeds up production and has high financial savings ([28]). Furthermore, things like cooling channels, feed lines and other inner geometry that would require additional post-processing will be integrated without more spending.

Depending on the size of the part to be produced, there are a few options to create it

using metal AM.

Selective laser melting (SLM) is the process of putting down thin layers of metal dust and melting the parts cross section on it, moving up one layer and repeating the process to manufacture the finished product. SLM has the highest precision of the metal AM technologies but it has its drawbacks. Low material deposition rates due to the use of one or more lasers and the granular approach of production and limited build volumes mean it is not the best for large scale systems. While this does limit SLM's use, the main advantage it has over other methods is its precision, capable of 0.1mm tolerances and creation of 0.6mm([30]) in diameter hole structures it cannot be replace as of this moment.

Direct energy deposition (DED) works with a free form tool path allowing more maneuverability and a much bigger work space. DED does compromise on tolerances when compared to SLM but the trade off is well worth it when larger parts are needed. If used in tandem with other techniques it may even be better than SLM ([31]).

To properly utilize AM for rocket engines it will be important to know what is being used for production due to size (SLM or DED). If micrometer precision is needed- AM may not be suitable. For SLM part orientation while printing is important because overhangs bigger than 45-50° will need supports of will fail otherwise. Lastly, the direction of manufacturing is of paramount importance as the AM as the strenght is not homogenous in diferent directions([32]).

To conclude the AM review, the looked at information indicates that AM is suitable for our engine design as it has been used in both tests and real missions ([28]). Further consideration will be given to the material compatibility between the mission, propellants used and manufacturability.

2.4   Metal compatibility with the propellants

The compatibility of each propellant with the container material is crucial in rocket technology. Serious issues start to arise because a considerable amount of propellants are quite reactive, and only a few building materials can effectively contain them. Many alloys resistance to fuels and oxidizers depends solely on the development of an inert, corrosion-resistant layer or barrier coating. The presence of various metals tends to encourage the disintegration of the propellant in addition to corrosion issues. Additionally, when hit, some metal/oxidizer combinations may ignite.

In this sense, metallic construction materials could be classified into 4 classes, out of which the first class exhibits a corrosion rate of less than 1mils/year and is free from impact sensitivity and class 4 materials would not be usable for such applications. Thus, it is only Class 1 metallic materials that are to be considered for the manufacturing of the engine itself.

Table 2.2: Compatibility classification for metals [15]

CORROSION RESISTANCE

Class	Rating	Penetration rate [$mils/s$]	Decomposition of propellant	Shock sensitivity
1	Excellent	< 1	No	No
2	Good	< 5	No	No
3	Fair	5 to 50	Some	No
4	Poor	> 50	Extensive	Yes

The compatibility rating for metals with MMH or NTO is primarily an indication of the degree to which the metal affects the propellant, since non-contaminated hydrazine has little effect on metals. The metals with best corrosive behavior when in contact with MMH are several aluminum alloys, stainless steels and miscellaneous metals (titanium, zirconium, platinum...), almost coincident with the ones for nitrogen-tetroxide.

Contrary to the usual toxic propellant couple, if corrosion of H_2O_2 takes place, usually the hydrogen peroxide will also decompose, although the reverse is not true. Higher strength peroxide (98%) is, in general, more stable with aluminum alloys, out of whom Al 1060 is widely spread among industrial or aerospace applications. This behavior is valid under low temperature conditions. A specific test campaign would be needed to check the compatibility in case of an environment such as the one existent within a combustion chamber. Similar metals as the one stated for hydrazine fuel can be employed when manufacturing kerosene-type pressure tanks or combustion chambers, however with slight differences. Based on the previous information, the following material choice has been made for each of the propellant couples:

Table 2.3: Aluminum 6061 mechanical properties [17]

Details	Values
Tensile strength	310 MPa
Yield strength	276 MPa
Modulus of elasticity	68.9 GPa
Density	2700 kg/m^3

- **Toxic propellant couple:**
  Both the fuel and oxidizer tanks are made of aluminum alloy 6061 due to its compatibility with both MMH and NTO. It is an aluminum-based alloy that stands-out for its thermal conductivity, workability and strength, while still being light weight and corrosion-resistant. Table 2.3 lists the mechanical characteristics of aluminum 6061.

In order to prevent catastrophic failure of the thrust chamber or nozzle, which are

subjected to intense heat and pressure during thrusting, a particular high temperature material is required. Alloys made of columbium, titanium, iridium, rhenium, tantalum, and rhodium are a few examples of high temperature metal alloys. The selected choice for the toxic couple case is a sort of titanium alloy, Ti-6Al-4V, due to its compatibility with such propellant as well as additive manufacturing techniques. It has a high strength at high temperatures (melting point at $\sim 1600^{\text{o}}$C) and is relatively light in weight.

Table 2.4: Titanium Ti-6Al-4V mechanical properties at a temperature $\sim 1000^{\text{o}}$C [18]

Details	Values
Tensile strength	950 MPa
Yield strength	880 MPa
Modulus of elasticity	114 GPa
Density	4430 kg/m^3

- **Non-toxic propellant couple:** Due to its former application in aerospace industry and the compatibility with both the oxidizer and fuel, Al 6061 will be implemented for the pressure tanks. This selection, instead of the mentioned Al 1060, has been done as it offers better properties and in the meanwhile it allows to shorten the breach between toxic and non-toxic designs.

Inconel X-750 is a nickel-chromium alloy that is commonly used for rocket engine thrust chambers. The high strength and corrosion resistance of Inconel X-750 make it a popular material choice for these demanding and high-temperature environments. Moreover, Inconel X-750 is compatible with additive manufacturing techniques, such as selective laser melting (SLM), laser powder bed fusion (LPBF), and electron beam melting (EBM), among others.

Table 2.5: Inconel X-750 mechanical properties

Details	Values
Tensile strength	1120 MPa
Yield strength	760 MPa
Modulus of elasticity	161 GPa
Density	8280 kg/m^3

Chapter 3

Engine Design

3.1 Combustion Design

NASA CEA code ([20]) is exploited to design and solve the combustion problem, using a frozen model with the input in table 3.1, and assuming an infinite area for the combustion chamber.

Table 3.1: Input values for the toxic N_2O_4 and MMH propellant

ϵ [-]	p_c [bar]	$T_s[K]$
200	10	298.15

The optimal mixture ratio is chosen by taking the one OF that maximize the specific impulse computed by the software, taken only as a reference to perform the decision. In figures 3.1 and 3.2 it is possible to see the influence of the ratio on the specific impulse.
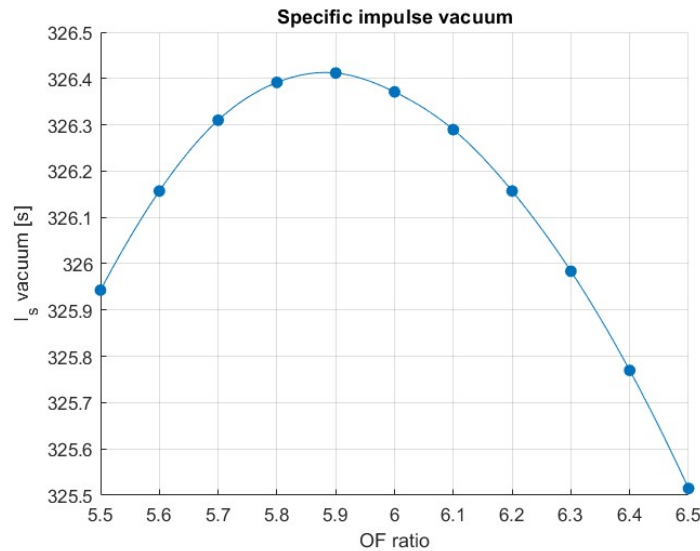

Figure 3.1: Specific impulse as a function of OF ratio of the green couple
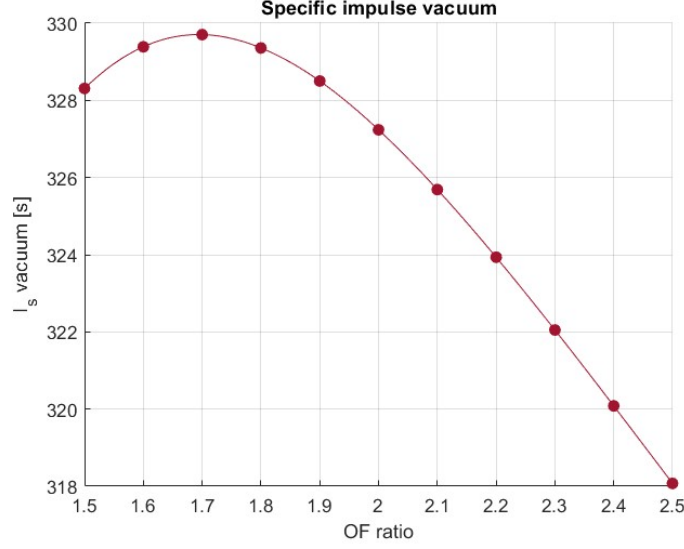
Figure 3.2: Specific impulse as a function of OF ratio of the toxic couple

The OFs are determined with an accuracy of *0.01* and the resulting ratios are *1.69* for the toxic couple and *5.88* for the green one. These values will be used for the nominal design and for the up- and down-scaling of the engines.

3.2   Nozzle design

The nozzle design will be carried out considering several assumptions: mono-phase, non-reacting (frozen), isentropic flow, perfect gas and quasi 1D gas dynamics. Moreover, the preliminary nozzle designed will be conical-shaped.

The NASA CEA Code ([20]) is again used to obtain the properties of the propellant couples in terms of density, dynamic viscosity and specific heat ratio at the optimal OF ratio.

Table 3.2: CEA data of the propellants

	$\rho_{prop}\,[kg/m^3]$	$\mu_{prop}\,[Pa \cdot s]$	γ [-]	$T_c\,[K]$	$M_{mol}\,[kg/kmol]$
MMH+NTO	0.8050	$0.9602 \cdot 10^{-4}$	1.2313	3079.67	20.613
RP-1+H₂O₂	0.9081	$0.9804 \cdot 10^{-4}$	1.1856	2810.88	21.223

Before fixing the geometry, it is necessary to solve the isentropic equations regarding the nozzle (considering all the stated assumptions) which will provide the results for the propellant mass flow rate and all the performance parameters. Equations can be found in appendix A.1. The results are shown in the following table 3.3 where $D_c = 0.0430\,m/s$.

Table 3.3: Nozzle performance and geometrical properties for both propellants.

Propellant	$p_e\,[Pa]$	$v_e\,[m/s]$	c_T	$\dot{m}\,[kg/s]$	$D_t\,[m]$	$D_e\,[m]$
MMH+NTO	234.47	3236.4	1.95	0.1447	0.0177	0.2505
RP-1+H$_2$O$_2$	299.08	3181.2	2.02	0.1464	0.0174	0.2462

3.2.1 Conical nozzle

The size of the nozzle is computed considering the 1D reference thrust. Then, once the conical geometry is selected, the 2D thrust level will be obtained from it, correcting the 1D model result. In a conical nozzle, there are two design angles (α,β) defining the angle from throat to exit and from chamber to throat respectively. These will be fixed to typical values $\alpha = 15^{\mathrm{o}}$ and $\beta = 45^{\mathrm{o}}$. Thanks to the former, the coefficient representing the losses due to the bidimensionality of the flow λ_{2D} can be computed.

$$\lambda_{2D} = \frac{1 + \cos(\alpha)}{2} \tag{3.1}$$

which only affects the momentum contribution

$$T_{2D} = \lambda_{2D}\dot{m}v_e + A_e \cdot p_e \qquad I_{s,2D} = \frac{T_{2D}}{g_0\dot{m}} \tag{3.2}$$

as longs as $p_a = 0$ due to being in vacuum.

These computations are consistent with the 1D model and 2D correction. The specific impulse computed using the CEA code is merely a reference value, making consistent the results.

Finally, the geometry design is finished by computing the different lengths defining the engine, equations shown in A.2.

3.2.2 Rao Approximation

A more complex construction, which however reduces the divergence losses, is a bell geometry one computed thanks to Rao approximation. This process makes use of an $\alpha = 15^{\mathrm{o}}$ reference conical nozzle (the one implemented before) to compute a reference divergent part length. This length will be modified by multiplying by a percentage, which is going to be fixed to $L_{Rao} = 100\,\%L_{div,conic15}$ since it maximizes the performance (in consonance with the selection of I_s) and there is no constraints in the weight of the system.

Looking at the figure A.1 from appendix A.4 it is possible to obtain the geometric constraints of the Rao nozzle starting from the expansion area ratio (the same used in the conic design) and the percentage previously chosen, leading to both θ_i and θ_e. See the redefinition of corresponding losses at appendix A.4. For the case of analysis, since the choice of the percentage with respect to the reference conical is 100%, for the selected ϵ the resulting angles are: $\theta_i = 33.8\,[^{\mathrm{o}}]$ and $\theta_e = 4.7\,[^{\mathrm{o}}]$. The results concerning both geometries are shown in the table below 3.4:

Table 3.4: Nozzle geometrical properties for the toxic NTO and MMH and non-toxic H_2O_2 and RP1 (kerosene) propellant

Propellant	Conic nozzle						Bell nozzle			
	$L_{conv}\,[m]$	$L_{div}\,[m]$	L_{conic}	λ	$T_{2D}\,[N]$	$I_s\,[s]$	$L_{Rao}\,[m]$	λ	$T_{2D}\,[N]$	$I_s\,[s]$
MMH+NTO	0.0126	0.4344	0.4471	0.9830	472.02	332.54	0.4344	0.9926	476.55	335.75
RP-1+H$_2$O$_2$	0.0125	0.4268	0.4393	0.9830	472.06	328.78	0.4268	0.9926	476.57	331.91

3.2.3 Shapiro model

The relationships that have been employed up to this point to size the nozzle are predicted on the idea of an isentropic flow, in which the system's energy is conserved. In practice, the exhausted gases' friction as they move through the duct results in energy losses inside the flow, which are manifested by a total pressure drop. The Shapiro model is used to analyse how friction impacts the propulsion system's performance in the case of the conic design. The fluctuations of the Mach number, static pressure, and sound speed with respect to the x coordinate (the origin is chosen at the beginning of the convergent region of the nozzle) are analysed specifically under the assumption of a quasi-1D flow based on the following equations:

$$\frac{dM^2}{dx} = \left\{ -2\frac{[1 + \frac{\gamma-1}{2}M^2]}{1-M^2}\frac{1}{A}\frac{dA}{dx} + \frac{\gamma M^2[1 + \frac{\gamma-1}{2}M^2]}{1-M^2} \cdot 4\frac{C_f}{D} \right\} M^2 \qquad (3.3)$$

$$\frac{dp}{dx} = \left\{ \frac{\gamma M^2}{1-M^2}\frac{1}{A}\frac{dA}{dx} - \frac{\gamma M^2[1 + (\gamma-1)M^2]}{2(1-M^2)} \cdot 4\frac{C_f}{D} \right\} p \qquad (3.4)$$

$$\frac{da}{dx} = \left\{ \frac{\frac{\gamma-1}{2}M^2}{1-M^2}\frac{1}{A}\frac{dA}{dx} - \frac{\gamma(\gamma-1)M^4}{4(1-M^2)} \cdot 4\frac{C_f}{D} \right\} a \qquad (3.5)$$

Notice how the heat exchange is not considered in such analysis, and only area variation of the nozzle and friction contributions are considered. C_f is the Fanning friction factor which can be obtained roughly from the Moody diagram as a function of the Reynolds (Re) number and the relative pipe roughness (ϵd, assumed a value of $40\mu m$), which is estimated based on the metals the nozzle is made of and the additive manufacturing technique employed. Both these figures change along the nozzle. Hence, two average values are fixed for the convergent and divergent part respectively, while γ is assumed constant.

The term $\frac{dA}{dx}$ is known as far as the nozzle geometry for the conic case is defined as:

$$A_{conv}(x) = \pi[R_t + (L_{conv} - x)\tan(\beta)]^2 \qquad 0 < x < L_{conv} \qquad (3.6)$$

$$A_{div}(x) = \pi[R_t + (x - L_{conv})\tan(\alpha)]^2 \qquad L_{conv} < x < L_{tot} \qquad (3.7)$$

In order to show some results obtained with this more advanced model and demonstrate the effect of friction, the results concerning the non-toxic propellant are shown below. As it can be seen the thrust will be reduced since the exit velocity of the exhausted gases from the divergent part will decrease with respect to the isentropic model. In fact, the exit velocity in this case, reaches a value $v_e = M_e \cdot a_e = 2.9621e + 03\,m/s$ which is a noticeable decrease of the isentropic value.
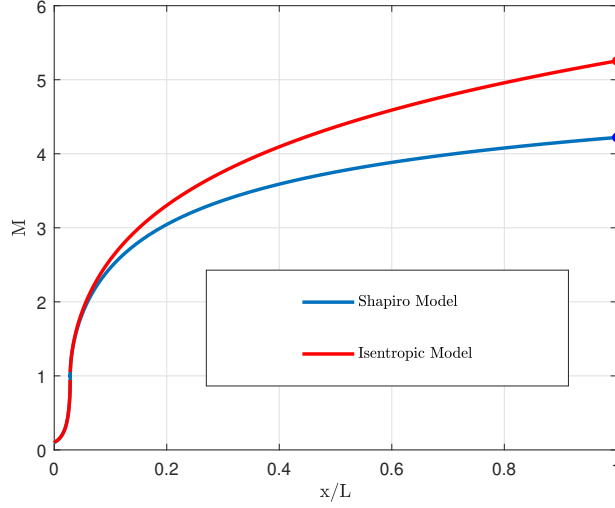
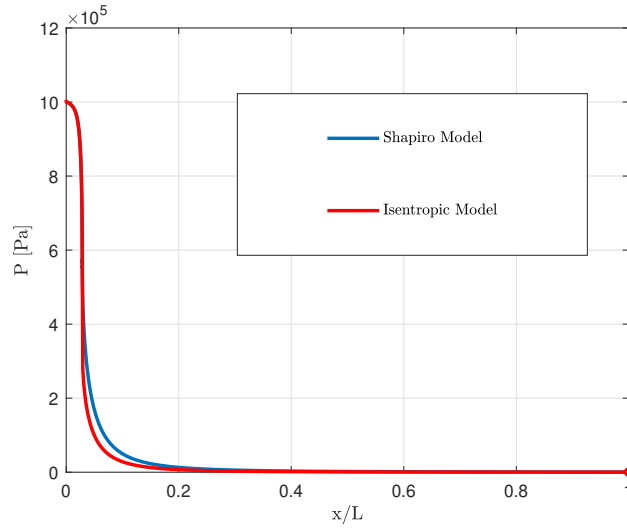Figure 3.3: Mach number evolution at the nozzle comparing Shapiro versus Isentropic model.

Figure 3.4: Pressure evolution at the nozzle comparing Shapiro versus Isentropic model.

3.3 Combustion Chamber geometry

Once the throat area and mass flow rate have been determined it is possible to design the geometry of the combustion chamber. The characteristic lengths, [14] allow to determine the chamber volume. Knowing the flow properties in the chamber, imposing a Mach number of *0.1* to grant an adequate combustion and using the continuity equation the remaining geometric parameters are found, as seen in A.3. For the two couples the values obtained are:

Table 3.5: Geometrical parameters of the combustion chamber

	$L^*\,[m]$	$V_c \cdot 10^{-4}\,[m^3]$	$A_c \cdot 10^{-3}\,[m^2]$	$D_c \cdot 10^{-2}\,[m]$	$L_c\,[m]$
MMH+NTO	0.825	2.03	1.45	4.30	0.14
RP-1+H$_2$O$_2$	1.65	3.93	1.41	4.24	0.28

3.4 Injection design

The design of the injectors starts from the imposition of the holes' diameter, taken as *1 mm* in all the cases; this constraint comes from the manifacturing technology limits. Then the configuration is chosen looking at the OF; for the hypergolic couple a "like-on-like" doublets configuration is selected in order to avoid proximity of the flame front relatively to the injector plate; the non-toxic couple requires a pentad unlike arrangement given the high OF. The angles of the injectors with respect to the axial direction are 45°, a reasonable value considering the manifacturing technology.

Table 3.6: Injectors configuration and performance

Propellant	Fuel injectors					Oxidizer injectors					Grouping	Type
	$\dot m_{FU}[\frac{g}{s}]$	$N[-]$	$\frac{\Delta P}{Pc}[-]$	$v[\frac{m}{s}]$	$\theta_{inj}[°]$	$\dot m_{OX}[\frac{g}{s}]$	$N[-]$	$\frac{\Delta P}{Pc}[-]$	$v[\frac{m}{s}]$	$\theta_{inj}[°]$		
MMH+NTO	53.8	6	15.2%	13.1	45	90.9	8	14.5%	10.1	45	Like	Doublet
RP-1+H$_2$O$_2$	21.3	2	22.8%	16.5	0.0	125	8	27.9%	13.7	45	Unlike	Pentad

3.5 Heat transfer analysis

Before proceeding, it is important to remark that some stress analysis has been performed, in particular the minimum thickness to support the cylindrical pressure load and the maximum thickness needed for regenerative cooling. The first is detailed only in the appendix section, and the second is not, as both chamber materials have high thermal conductivity and it was decided to use generative cooling only on the initial part of the combustion chamber. This section is dedicated to the heat transfer calculation, and in the next sections the cooling strategies will be discussed and further elaborated.

To have a good estimate of the heat flux distribution along the engine walls, the geometry of the conical nozzle was discretized in one thousand equally sized slices (Fig. B.7) before applying the equations of isentropic expansion, for each propellant and scaling version. Numerous figures have been produced but only the most relevant ones, are shown next. For the interest of the reader, the complete collection can be found in the appendix. In this section the thermal analysis will be further restricted to the MMH+NTO nominal case.

After discretizing, solving the isentropic expansion provides access to essential parameters such as the Mach number, fluid velocity, speed of sound, static pressures, temperatures, and densities, along with the constants c_p and γ. The procedure follows by modeling the dynamic viscosity μ using Sutherland's law[A.20], Re and Pr numbers[A.21t],

the stagnation temperature T_0, the factor of recovery R and finally the adiabatic wall temperature.[A.22]

The heat flux can now be computed with the following formula:

$$\dot{q} = h_g(T_{aw} - T_w) \tag{3.8}$$

The transfer coefficient h_g can be approximated using several different approaches, but the Bartz model[23] has ended up being chosen over others like Dittus-Boelter due to its better accuracy.

$$h_g = \frac{0.026}{D_t^{0.2}} \left(\frac{\mu^{0.2}}{Pr^{0.6}} c_{pg}\right) \left(\frac{p_c}{c^*}\right)^{0.8} \left(\frac{D_t}{r_{curv}}\right)^{0.1} \left(\frac{A_t}{A}\right)^{0.9} \sigma \tag{3.9}$$

$$\sigma = \frac{1}{\left(0.5\frac{T_w}{T_{aw}}\left(1 + \frac{\gamma-1}{2}M^2\right) + 0.5\right)^{0.68} \left(1 + \frac{\gamma-1}{2}M^2\right)^{0.12}} \tag{3.10}$$

T_w is the maximum imposed temperature that the hot side of the wall can have. For the toxic couple this is $700°C$ and for the non-toxic couple this is $922°C$. These values where found in literature.[18][25] The resulting heat flux in the analyzed case (other cases are similar) remains nearly constant in the CC, peaks at the throat and exponentially decays towards the exit, as it can be observed in Fig. 3.5. The area is much larger in the exit section of the chamber, so when the flux is added up in each discretized slice, the curve flattens, but it still conserves its shape. Total heat flux was calculated by summing these results, reaching 127kW. Figures can be found in the appendix.
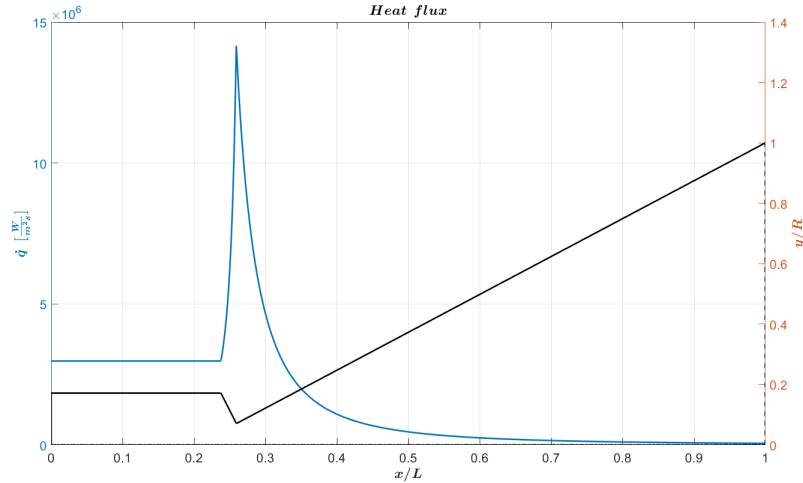

Figure 3.5: Pointwise heatflux for the MMH+NTO propellants and nominal thrust case

3.5.1 Ablative cooling

Ablative cooling is a simple and low-cost method to cool down the engine. It cools down the engine by heating up and evaporating the ablative layer, when the evaporated material is ejected out of the nozzle it takes an amount of excess heat with it. The biggest problem with ablative cooling however is that the diameter of the different parts of the engine are changing with time. According to a paper published by NASA [22], the change of the

radius is around *4-5mm* each two minutes. This will result in a total change in diameter of around *150mm* after thirty minutes. This is obviously way to much, and for this reason ablative cooling will not be used.

3.5.2 Heat sink

A heat sink is another option to prevent the engine from melting. However for a heat sink to work effectively, the chamber walls need to be thicker. This will result in an increase of weight. Heat sinks are also only effective for a shorter period of time depending on how thick the walls are. For these reasons a heat sink will also not be used.

3.5.3 Regenerative cooling

Regenerative cooling uses a coolant fluid that runs through channels on the outside of the engine and continuously cools down the walls to make sure it doesn't go over the maximum allowed temperature. The coolant also has a limit, which is usually related to the onset of boiling or decomposition into gas or carbon deposits. With the limits, it is possible to calculate the maximum amount of heat that can possibly be removed by each coolant:[A.25]

Table 3.7: Possible removed heat in the nominal case

Coolant	$Q_{regen,max}[kW]$
MMH	11.2
NTO	0.05
RP-1	9.5
H_2O_2	43.9

Based on these results it was decided to use the hydrazine in the hypergolic case, and the peroxide in the second case as coolant. Expressions for the c_p of the liquid phase, as a function of temperature, and maximum temperature for each liquid, as a function of pressure, are detailed in the equations section of the appendix. In all cases the regenerative cooling alone was not enough to offset the chamber heat flux.

3.5.4 Liquid film cooling

Holes provided in the combustion chamber walls can introduce a liquid coolant. This coolant will create a liquid film on the walls of the combustion chamber which will decrease the heat flux through the wall. When the coolant heats up it will start to vaporize creating an extra layer of gaseous coolant. The film flow rate can be calculated using formula 3.8. Using formulas 3.13, 3.11 and the values in table 3.9 the required mass flow rate of the coolant can be determined.[23]

$$\frac{G_c}{G_g} = \frac{1}{\eta} \cdot \frac{H}{2/f} \tag{3.11}$$

$$H = \frac{c_{pvc}(T_{aw} - T_w)}{c_{plc}(T_w - T_s) + \Delta H_{vc}} \tag{3.12}$$

$$\frac{1}{\sqrt{f}} = -2log_{10}\left(\frac{roughness = 25\mu_m}{3.7} + \frac{2.51}{Re\sqrt{f}}\right) \qquad (3.13)$$

The different parameters required in the formula are calculated for a small section of the engine each iteration. In table 3.8 and 3.9 the parameters are listed for the combustion chamber, throat and nozzle exit locations. The resulting mass flow rates of the liquid film cooling in the different sections are also listed in these tables.

Table 3.8: Liquid film cooling local thermal parameters for the NTO and MMH propellant

Location	$T_{aw}[K]$	$T_w[K]$	$T_s[K]$	$c_{plc}[\frac{J}{kgK}]$	$c_{pvc}[\frac{J}{kgK}]$	$c_{pg}[\frac{J}{kgK}]$	$f[-]$	$\dot{m}_{film}[\frac{g}{m^2s}]$
CC	3079	700	298.15	2974	2700	2147	0.0233	11.78
Throat	3007	700	298.15	2973	2700	2147	0.0232	11.23
Exit	2179	700	298.15	2967	2700	2147	0.0264	6.85

Table 3.9: Liquid film cooling thermal parameters for the RP-1 and H_2O_2 propellant

Location	$T_{aw}[K]$	$T_w[K]$	$T_s[K]$	$c_{plc}[\frac{J}{kgK}]$	$c_{pvc}[\frac{J}{kgK}]$	$c_{pg}[\frac{J}{kgK}]$	$f[-]$	$\dot{m}_{film}[\frac{g}{m^2s}]$
CC	2811	922	298.15	2332	3500	2503	0.0233	9.56
Throat	2803	922	298.15	2328	3500	2503	0.0231	9.49
Exit	2211	922	298.15	2230	3500	2503	0.0275	8.12

The final approach consisted in a combined cooling, using as much regenerative as possible in the beginning of the chamber and then switching to film cooling, as it can be seen in the figure 3.6.
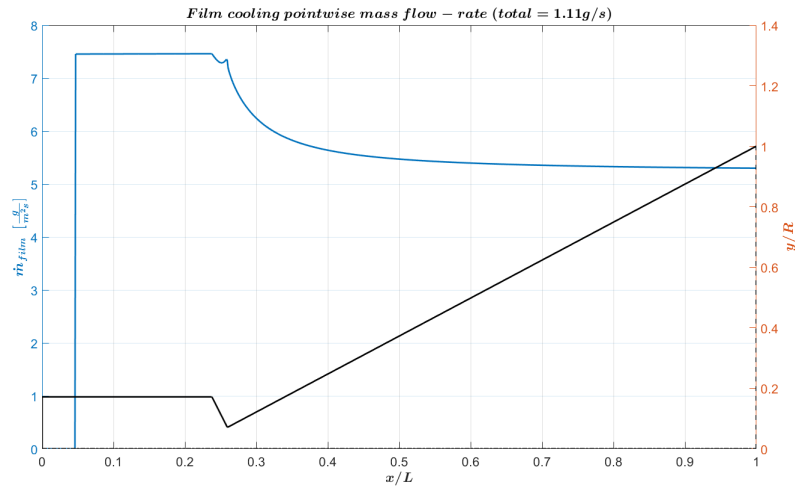

Figure 3.6: Pointwise film flux and total mass flow for the MMH+NTO propellants and nominal thrust case

Instead of keeping them separate, when these cooling methods are combined throughout the entire engine, a very small decrease in liquid film coolant mass flow rate is noticed.

However combining these methods throughout the engine results in a much more complex cooling system, especially for the green couple where the film coolant is different from the regenerative coolant. Therefore the cooling methods are kept separate.

3.6 Pressure-fed system

The pressurizing strategy adopts a pressure-fed system, Fig. 3.7, that allows to maintain a constant level of pressure in the chamber and so a constant thrust profile. The fuel and the oxidizer are pressurized by a gas contained in one high-pressure tank and a pressure regulator, placed before each tank, controls the pressure level to feed to the tanks.
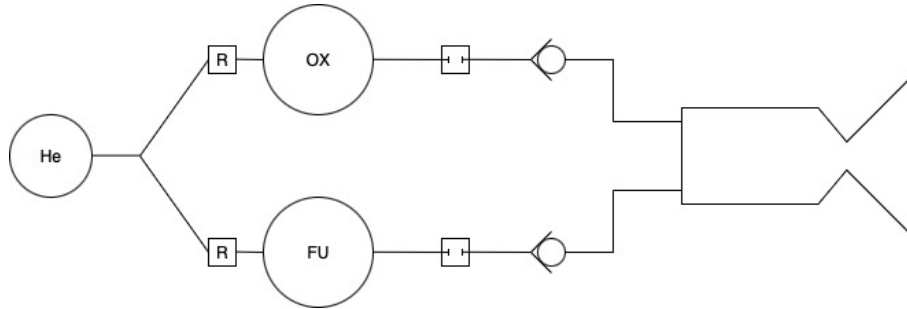
Figure 3.7: Pressure-fed system architecture

The gas chosen for the pressurization system is Helium, commonly used for its low weight, although being an expensive alternative with respect to other gases.

Table 3.10: Helium properties [21]

R [J/kgK]	γ [-]
2077.3	$\frac{5}{3}$

The design of the tanks needs to take into account the pressure losses along the feeding lines. All the formulas and coefficients will be taken from [24] and procedure shown in A.5. Starting from the sizing of the propellants' tanks these losses have to be computed taking as assumptions the diameter and length of the pipes. The distributed losses coefficient are obtained using the following approximation valid for smooth pipes and for Reynolds number between 4000 and 100000:

$$\lambda = \frac{0.316}{Re^{0.25}} \tag{3.14}$$

While the concentrated losses are due to the presence of the latch and check valves, modeled as orifices with the same diameter of the pipes, with the k coefficient taken equal to two, and the access to the feeding lines from the tanks, modeled as slightly rounded entrances, with th k coefficient taken equal to 0.25. The dimensions taken for the pipes are showed in table 3.11 and after having checked that the discharge velocities respect the typical limits for these applications (<10 m/s), the losses are computed for the different cases and so the pressures needed inside the tanks are computed, considering the losses due to the injection.

Table 3.11: Pipes geometry

	D [m]	L [m]
MMH feed line	0.004	0.58
NTO feed line	0.004	0.30
RP-1 feed line	0.004	0.30
H_2O_2 feed line	0.004	0.86

Once the tanks pressures are known, it's possible to design the tanks, assuming the shape as spherical and knowing the mass amount of the propellants and their densities, together with density and the yield strength of the material chosen (Al 6061). An increase in the propellant mass is implemented to take into account the budget needed for the film cooling. The results for each case are shown below.

Table 3.12: Tanks' parameters

	MMH	NTO	RP-1	H_2O_2
p_t [bar]	12.335	12.484	12.408	15.889
m_p [kg]	108.564	178.453	62.687	246.787
V_{tank} [m^3]	0.124	0.123	0.079	0.174
m_{tank} [kg]	2.262	2.271	1.434	4.050

The upstream line, inside which flows a gas stream, will not see a pressure losses computation, but the design will consider a reasonable margin to size the helium tank. The pressure inside the helium tank at the end of the burning must be at least equal to the greater between the two propellants tanks, to which is added a reasonable margin of 10% for security reason and to consider the losses on the line. From that the pressure prior to the starting of the combustion is imposed as 10 times the final pressure. Now assuming the flow as adiabatic, it's possible to retrieve the mass of helium needed for the pressurization and the volume of its tank:

The tank of the pressurizing gas shape and material is taken as the ones for the propellants. Using the same formulas seen above the pressurizing tank parameters are:

Table 3.13: Pressurizing tank's parameters

	MMH+NTO	RP-1+H_2O_2
$p_{press,in}$ [bar]	124.84	158.89
m_{He} [kg]	0.666	0.860
$V_{tank,He}$ [m^3]	0.083	0.084
$m_{tank,He}$ [kg]	1.746	2.511

Chapter 4

Engine scaling and comparison

The scaling problem has been approached maintaining the same pressure inside the chamber and expansion ratio for the nozzle. In this way the change of the thrust level varies the geometry of the engine and the mass flow rate, and at the same time the burning time needed to accomplish the Δv required. The procedure followed it's the same illustrated in Chapter 3 and the main results of the analysis are reported.

4.1   Nozzle design

Table 4.1: Nozzle geometrical properties

Propellant	Scaling	$D_t\,[m]$	$D_e\,[m]$	Conic nozzle			Bell nozzle		
				$L_{conv}\,[m]$	$L_{div}\,[m]$	L_{conic}	$\theta_i\,[^\text{o}]$	$\theta_e\,[^\text{o}]$	$L_{Rao}\,[m]$
MMH+NTO	Half Thrust	0.0125	0.1771	0.0152	0.3072	0.3224	33.8	4.7	0.3072
	Double Thrust	0.0251	0.3543	0.0090	0.6144	0.6233	33.8	4.7	0.6144
RP-1+H$_2$O$_2$	Half Thrust	0.0123	0.1741	0.0150	0.3018	0.3169	33.8	4.7	0.3018
	Double Thrust	0.0246	0.3481	0.0089	0.6037	0.6125	33.8	4.7	0.6037

Table 4.2: Nozzle performance properties

Propellant	Scaling	c_T	$\dot{m}\,[kg/s]$	Conic nozzle			Bell nozzle		
				λ	$T_{2D}\,[N]$	$I_s\,[s]$	λ	$T_{2D}\,[N]$	$I_s\,[s]$
MMH+NTO	Half Thrust	1.95	0.0724	0.9830	236.010	332.54	0.9926	238.27	335.73
	Double Thrust	1.95	0.2895	0.9830	944.04	332.54	0.9926	953.09	335.73
RP-1+H$_2$O$_2$	Half Thrust	2.02	0.0732	0.9830	236.03	328.78	0.9926	238.28	331.91
	Double Thrust	2.02	0.2928	0.9830	944.13	328.78	0.9926	953.13	331.91

4.2   Combustion Chamber geometry

While the length of the chamber remains unvaried, the volume and the area change linearly. This doesn't constitute a problem in terms of feasibility, but will involve weight change in the two cases.

Table 4.3: Chamber geometrical parameters for the scaled engines

Propellant	Scaling	$V_c \cdot 10^{-4}\,[m^3]$	$A_c \cdot 10^{-3}\,[m^2]$	$D_c \cdot 10^{-2}\,[m]$	$L_c\,[m]$
MMH+NTO	**Half Thrust**	1.02	0.73	3.04	0.14
	Double Thrust	4.07	2.91	6.08	0.14
RP-1+H$_2$O$_2$	**Half Thrust**	1.96	0.71	0.30	0.28
	Double Thrust	7.85	2.82	6.00	0.28

4.3   Injection design

When scaling the designs, in regards to injection, it was decided to double or halve the injection area by doing the same to the number of injectors.

Table 4.4: Downscaling - Injectors configuration and performance

Propellant		Fuel injectors					Oxidizer injectors				Grouping	Type
	$\dot{m}_{FU}[\frac{g}{s}]$	$N[-]$	$\frac{\Delta P}{Pc}[-]$	$v[\frac{m}{s}]$	$\theta_{inj}[°]$	$\dot{m}_{OX}[\frac{g}{s}]$	$N[-]$	$\frac{\Delta P}{Pc}[-]$	$v[\frac{m}{s}]$	$\theta_{inj}[°]$		
MMH+NTO	26.9	3	15.2%	13.1	45	45.5	4	14.9%	10.1	45	Like	Triplet & Doublet
RP-1+H$_2$O$_2$	10.6	1	22.8%	16.5	0.0	62.6	4	27.9%	13.7	45	Unlike	Pentad

Table 4.5: Upscaling - Injectors configuration and performance

Propellant		Fuel injectors					Oxidizer injectors				Grouping	Type
	$\dot{m}_{FU}[\frac{g}{s}]$	$N[-]$	$\frac{\Delta P}{Pc}[-]$	$v[\frac{m}{s}]$	$\theta_{inj}[°]$	$\dot{m}_{OX}[\frac{g}{s}]$	$N[-]$	$\frac{\Delta P}{Pc}[-]$	$v[\frac{m}{s}]$	$\theta_{inj}[°]$		
MMH+NTO	108	12	15.2%	13.1	45	182	16	14.9%	10.1	45	Like	Doublet
RP-1+H$_2$O$_2$	42.5	4	22.8%	16.5	0.0	250	16	27.9%	13.7	45	Unlike	Pentad

4.4   Heat transfer analysis

for the liquid film cooling only a number of parameters are changed by the scaling, these parameters are listed in table 4.6 for comparison.

Table 4.6: Cooling system parameters for the scaled engines

Propellant	Scaling	$L_{regen}\,[m]$	CC		Nozzle		Exit	
			$f\,[-]$	$\dot{m}_{film}\,[\frac{g}{m^2 s}]$	$f\,[-]$	$\dot{m}_{film}\,[\frac{g}{m^2 s}]$	$f\,[-]$	$\dot{m}_{film}\,[\frac{g}{m^2 s}]$
MMH+NTO	**Half Thrust**	0.019	0.0253	6.4	0.0253	6.3	0.0288	3.7
	Double Thrust	0.04	0.0214	21.7	0.0213	21.2	0.0242	12.7
RP-1+H$_2$O$_2$	**Half Thrust**	0.09	0.0253	37.9	0.0255	38.27	0.0301	27.14
	Double Thrust	0.194	0.0214	129.1	0.0214	128.2	0.0252	89.09

The regenerative cooling system is separated from the film cooling just as in the nominal case. L_{regen} indicates the length of the regenerative cooling system.

4.5 Pressure-fed system

Changing the thrust required clearly changes the sizing of the propellant tanks and the design of the pressurization system. These changes are summed up in the following tables:

Table 4.7: Tank parameters

Scaling	Tank	p_t [bar]	m_p [kg]	V_{tank} [m^3]	m_{tank} [kg]
Half Thrust	MMH	11.744	111.531	0.128	2.212
	NTO	11.754	178.453	0.124	2.138
	RP-1	12.328	83.403	0.105	1.895
	H_2O_2	13.646	246.787	0.174	3.477
Double Thrust	MMH	14.527	107.079	0.124	2.628
	NTO	15.286	178.453	0.124	2.782
	RP-1	12.747	52.329	0.066	1.229
	H_2O_2	24.093	246.787	0.175	6.151

Table 4.8: Pressurizing tank parameters

Scaling	Tank	$p_{press,in}$ [bar]	m_{He} [kg]	$V_{tank,He}$ [m^3]	$m_{tank,He}$ [kg]
Half Thrust	MMH+NTO	117.54	0.636	0.084	1.659
	RP-1+H_2O_2	136.46	0.814	0.093	2.302
Double Thrust	MMH+NTO	152.86	0.810	0.083	2.130
	RP-1+H_2O_2	240.93	1.236	0.080	3.684

Chapter 5

Conclusions

5.1 Performances

When comparing the green versus the toxic propellant there are a number of variables that need to be compared to get a clear vision which type is best. The variables that will be checked are the specific impulse of each fuel type, the combustion chamber volume, the total mass flow rate and the liquid film coolant mass flow rate. In table 5.3 these values are listed for each couple as well as the scaling results.

Table 5.1: Final engine performance parameters.

Propellant	Scaling	$T[N]$	$I_s[s]$	$m_p[kg]$	$t_{burn}[min]$	$I_{tot}[N \cdot s]$
MMH+NTO	*Downscaled*	238.27	334.25	285.46	65.451	935700
	Nominal	476.55	333.17	286.39	32.726	935735
	Upscaled	953.09	331.21	288.08	16.363	935725
RP-1+H$_2$O$_2$	*Downscaled*	238.28	329.74	290.80	65.773	940.343
	Nominal	476.57	328.29	292.09	32.886	940349
	Upscaled	953.13	325.73	294.38	16.443	940339

As it can be noticed from the table 5.3 above, the specific impulses seem to go down as the engine is upscaled. This behaviour in first instance is opposed to what it was expected from the theoretical point of view. However, the effect of heating the coolant through regeneration was not counted and that could reverse the trend.

Regarding the values presented, it can be observed that in some cases, the ones corresponding to the toxic couple are better in term of this analysed performances wheres in others the green couple seem to be more appropiate. Thus, a trade off between them is required to decide which one to use. Therefore, it is finally presented the comparison between the green option and the standard toxic one. Therefore, the decision on this choice will be based on a trade-off between propellant weight, compactness, survivability of components/propellant, and production feasibility, which is now the task of the technical supervisor.

5.2 Manufacturability

When looking at all the substantial dimensions of all 6 engines, we can draw some conclusions. In case of the downscaled engines it would be possible to use a monolithic design for both propellant types, utilizing the more precise SLM process, saving both time and money. When moving up in scale, the aforementioned choice would be hard to realize due to SLM size limits. Because of that, the C.C. and nozzle could be split in to two parts or using DED (if the small element size allows it) we could still use a monolithic design with a considerable bump up in printing speed but the switch to DED would nescesitate a redesign of the injector hole size due to the worse precision. In case of the diameter of all the engines, there is no problem with SLM limitations in that regard.

Table 5.2: Dimension comparison

Propellant	Scaling	$L_{conv}[m]$	$L_{div}[m]$	$L_{engine}[m]$	$D_c[m]$	$D_t[m]$	$D_e[m]$
	Downscaled	0.0152	0.3072	0.4623	0.0304	0.0125	0.1771
MMH+NTO	*Nominal*	0.0126	0.4344	0.5870	0.0430	0.0177	0.2505
	Upscaled	0.0090	0.6144	0.7632	0.0608	0.0251	0.3543
	Downscaled	0.0150	0.3018	0.5953	0.0300	0.0123	0.1741
RP-1+H₂O₂	*Nominal*	0.0125	0.4268	0.7177	0.0424	0.0174	0.2462
	Upscaled	0.0089	0.6037	0.8909	0.0600	0.0246	0.3481

Although with the bigger scales there is a need to use multi-part assemblies, there are possible ways to join two AM part sections with precise wire fed welding robots to create a uniform, homogeneous bond but this method requires more research and experimentation.

5.3 Influence on mass budget

The scaling affects also the dry masses and the volumes needed for storing the propellants and the pressurizing gas. Increasing the thrust more dry mass will be requested by the system. Moreover the engines powered by the toxic couple present a lower volumetric impulse, resulting in more compact tanks, other than the upscaled engine.

Table 5.3: Dry masses and volumes comparison

Propellant	Scaling	$m_{dry} + m_{He}[kg]$	$V_{tanks}[m^3]$	$I_V[kg \cdot s/m^3]$
MMH+NTO	*Downscaled*	6.645	0.336	386393
	Nominal	6.945	0.330	386477
	Upscaled	8.350	0.331	384866
RP-1+H$_2$O$_2$	*Downscaled*	8.488	0.372	393380
	Nominal	8.855	0.337	405110
	Upscaled	12.300	0.321	409443

Bibliography

[1] *Apogee Kick Motor* (2022) Wikipedia. Wikimedia Foundation. `https://en.wikipedia.org/wiki/Apogee_kick_motor`

[2] *The Online Materials Information Resource.* `https://www.rocketlabusa.com/updates/the-kick-stage-responsible-orbital-deployment/`

[3] *Launch: Payload user's guide - August 2020 version 6.5 - rocket lab (no date) ReadkonG.com.* `https://www.readkong.com/page/launch-payload-user-s-guide-august-2020-version-6-5-7292873`

[4] *Lunar Photon Rocket Lab's Mission to the Moon.* `https://www.rocketlabusa.com/assets/Uploads/EXC22_017%20-%20Photon%20Doc_%C6%92%20[Web].pdf`

[5] *Ariane 6 targets new missions with Astris kick stage.* `https://www.esa.int/Enabling_Support/Space_Transportation/Ariane/Ariane_6_targets_new_missions_with_Astris_kick_stage`

[6] *Versatile, green rocket engine gets go-ahead from ESA.* `https://www.esa.int/Enabling_Support/Space_Transportation/Future_space_transportation/Versatile_green_rocket_engine_gets_go-ahead_from_ESA`

[7] Sutton, G.P. and Biblarz, O. (2017), *Rocket Propulsion Elements, Hoboken, NJ: John Wiley & amp; Sons, Inc.*

[8] Moon, Y. et al. (2014), *Design specifications of H2O2/kerosene bipropellant rocket system for space missions.* Aerospace Science and Technology, 33(1), pp. 118–121. Available at: https://doi.org/10.1016/j.ast.2014.01.006.

[9] Muhammad, N., Muhalim, F. B., and Krishnan, S. *Design of nitrogen-tetroxide/monomethyl-hydrazine thruster for upper stage application.* Department of Aeronautical Engineering. Universiti Teknologi Malaysia

[10] Matsumoto,J., Okaya S., Igoh H. and Kawaguchi J. (2017) *Concept of a self-pressurized feed system for liquid rocket engines and its fundamental experiment results.* Acta Astronautica V. 133

[11] Gordon, S. and McBride, B. J., *Computer Program for Calculation of Complex Chemical Equilibrium Composition, Rocket Performance, Incident and Refleted Shock and Chapman-Jouguet Detonations,* NASA SP-273, 1971.

[12] Carlotti, S. and Maggi, F. (2022), *Evaluating New Liquid Storable bipropellants: Safety and Performance Assessments.* Aerospace, 9(10), p. 561. Available at: https://doi.org/10.3390/aerospace9100561.

[13] United Nations Economic Commission for Europe. Secretariat. In Globally Harmonized System of Classification and Labelling of Chemicals (GHS); United Nations Publications: New York, NY, USA; Geneva, Switzerland, 2021.

[14] Maggi, F. Space Propulsion lectures, Politecnico di Milano, AY 2022-2023

[15] UNEY, P.E. and FESTER, D.A. (1972) *Material compatibility with Space Storable Propellants Design Guidebook.* Ft. Belvoir: Defense Technical Information Center

[16] Boyd, W.K., Berry, W.E. and White, E.L. (1965) *Compatibility of materials with rocket propellants and oxidizers.* Columbus, OH: Battelle Memorial Institute, Defense Metals Information Center.

[17] Bray, J. W., *Aluminium Mill and Engineered Wrought Products*, ASM Handbook, Vol. 2, pp. 27-61, ASM International, 2007.

[18] *ASM material data sheet.* https://asm.matweb.com/search/SpecificMaterial.asp?bassnum=mtp641

[19] *The Online Materials Information Resource.* https://www.matweb.com/search/datasheet.aspxmatguid=0df660ac8b87434ca82af7681a6098e1&ckck=1

[20] *NASA CEA.* https://cearun.grc.nasa.gov/

[21] *Pubchem website.* https://pubchem.ncbi.nlm.nih.gov

[22] *Ablative Material Testing for Low-Pressure, Low-Cost Rocket Engines* https://ntrs.nasa.gov/api/citations/19960007443/downloads/19960007443.pdf

[23] Dieter K. Huzel and David H. Huang, *Design of Liquid Propellant Rocket Engines*, NASA SP-125, 1967

[24] C. Cardani, Corso di Impianti e Sistemi Aerospaziali, Politecnico di Milano, AY 2020-2021

[25] *Inconel X-750 material data sheet* https://www.specialmetals.com/documents/technical-bulletins/inconel/inconel-alloy-x-750.pdf

[26] Anthony U. Akpati, SSME Main Combustion Chamber (MCC) Hot Oil Dewaxing.

[27] Julien Gardan, Additive manufacturing technologies: state of the art and trends, 2015.

[28] Paul Gradl, Sandy E. Greene. Additive Manufacturing of Liquid Rocket Engine Combustion Devices: A Summary of Process Developments and Hot-Fire Testing Results. 2018.

[29] Byron Blakey-Milner, Paul Gradl, Metal additive manufacturing in aerospace: A review. 2021.

[30] Laser Sintering Design Tips: Holes https://www.stratasys.com/en/stratasysdirect/resources/articles/ls-design-tips-holes/

[31] Wan-Sik Woo, Eun-Jung Kim, Ho-In Jeong, Choon-Man Lee. Laser-Assisted Machining of Ti-6Al-4V Fabricated by DED Additive Manufacturing. 2020

[32] William E. Frazier. Metal Additive Manufacturing: A Review. 2014.

Appendix A

Equations

A.1 Isentropic relationships

Assuming external vacuum conditions:

$$\frac{1}{\epsilon} = \left(\frac{k+1}{2}\right)^{\frac{1}{k-1}} \left(\frac{p_e}{p_c}\right)^{\frac{1}{k}} \sqrt{\frac{k+1}{k-1}\left[1 - \left(\frac{p_e}{p_c}\right)^{\frac{k-1}{k}}\right]} \tag{A.1}$$

$$c_T = \sqrt{2\frac{k^2}{k-1}\left(\frac{2}{k+1}\right)^{\frac{k+1}{k-1}}\left(1 - \left(\frac{P_e}{P_c}\right)^{\frac{k-1}{k}}\right) + \frac{P_e}{P_c}\epsilon} \tag{A.2}$$

$$c^* = \frac{\sqrt{T_c\,R}}{\Gamma(k)} \tag{A.3}$$

where $\Gamma(k)$ is the Vandekerckhove function $\Gamma(k) = \sqrt{k\left(\frac{2}{k+1}\right)^{\frac{k+1}{k-1}}}$

$$v_e = \sqrt{2\frac{k}{k-1}\frac{R}{M_{mol}}T_c\left(1 - \left(\frac{p_e}{p_c}\right)^{\frac{k-1}{k}}\right)} \tag{A.4}$$

$$A_t = \frac{T}{p_c\,c_T} \qquad D_t = 2\sqrt{\frac{A_t}{\pi}} \tag{A.5}$$

$$\dot{m} = \frac{p_c A_t}{c^*} \qquad \dot{m}_{Ox} = \frac{OF}{1+OF}\dot{m} \qquad \dot{m}_F = \frac{\dot{m}_{Ox}}{OF} \tag{A.6}$$

$$I_s = \frac{T}{\dot{m}g_0} \tag{A.7}$$

A.2 Geometry in conic nozzle

$$A_e = \epsilon\,A_t \qquad D_e = 2\sqrt{\frac{A_e}{\pi}} \tag{A.8}$$

$$
\left.\begin{array}{rcl}
L_{CONV} & = & \dfrac{r_c - r_t}{\tan(\beta)} \\[2mm]
L_{DIV} & = & \dfrac{r_e - r_t}{\tan(\alpha)}
\end{array}\right\} \qquad \longrightarrow \qquad L_{TOT} = L_c + L_{CONV} + L_{DIV} \qquad \text{(A.9)}
$$

A.3 Combustion chamber geometry

Having imposed $M_c = 0.1$ and $\dot{m} = \rho_c A_c v_c$, knowing the characteristic length for the chamber, the following are applied:

$$
v_c = M_c \cdot \sqrt{k \frac{R}{M_{mol}} T_c} \qquad \text{(A.10)}
$$

$$
A_c = \frac{\dot{m}}{\rho_c v_c} \qquad D_c = \sqrt{\frac{A_c}{\pi}} \qquad \text{(A.11)}
$$

$$
Vc = L^* \cdot A_t \qquad \text{(A.12)}
$$

$$
L_c = \frac{V_c}{A_c} \qquad \text{(A.13)}
$$

A.4 Rao Approximation
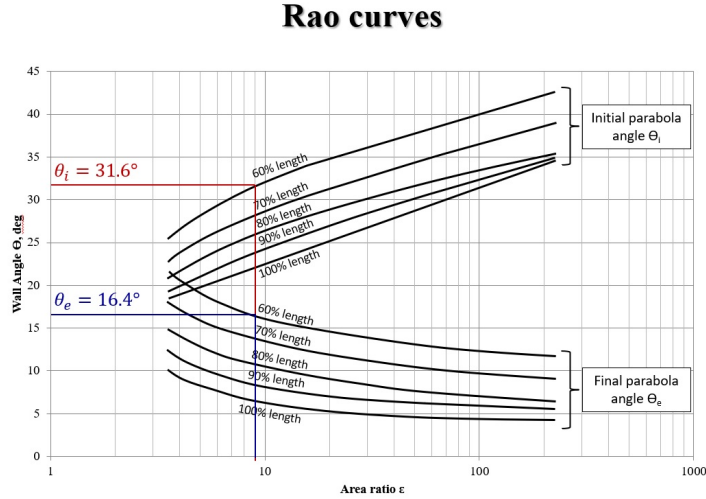
Figure A.1: Rao approximation.

The corresponding losses of such a nozzle design would be:

$$
\lambda_{Rao} = \frac{1 + \cos\left(\frac{\alpha + \theta_e}{2}\right)}{2} \qquad \alpha' = atan\left(\frac{D_e - D_t}{2L_{D,Rao}}\right) \qquad \text{(A.14)}
$$

A.5 Pressurization system

To compute the pressure losses along the line knowing the fluid properties and coefficients:

$$\Delta p_{distr} = \tfrac{1}{2}\lambda\tfrac{L}{D}\rho v^2$$

$$\Delta p_{conc} = \tfrac{1}{2}k\rho v^2 \tag{A.15}$$

For the helium tank the mass of gas needed and its volume are obtained:

$$m_{He} = \frac{1.1 \cdot p_t(V_{ox} + V_f)}{R_{He}T_t} \cdot \frac{\gamma_{He}}{1 - \frac{p_{press,in}}{p_{press,fin}}}$$

$$V_{press} = \frac{m_{He}R_{He}T_t}{p_{press,in}} \tag{A.16}$$

While the parameters of the tanks are calculated with the following:

$$r = \sqrt[3]{\frac{3V_t}{4\pi}}$$

$$t = \frac{p_t r}{2\sigma}$$

$$V_{tank} = \tfrac{4}{3}\pi((r+t)^3 - r^3) \tag{A.17}$$

$$m_{tank} = V_{tank}\rho_{Al}$$

A.6 Injectors design

Knowing the mass rate flowing through each hole, having imposed the diameter of injection, selected the discharge coefficient, the pressure losses due to the injection inside the chamber are determined:

$$A_{inj} = \pi\frac{D_{inj}^2}{4} \tag{A.18}$$

$$\Delta p = \left(\frac{\dot{m}}{c_D A_{inj}}\right)^2 \cdot \frac{1}{2\rho} \tag{A.19}$$

A.7 Thermal analysis formulas

The formulas required to determine the fluid flow parameters that are used in the thermal analysis. Sutherland's law. Sutherland's constants were estimated by evaluating the expression using CEA values of dynamic viscosity, from the throat to the exit point:
$(C_{MMH-NTO} = 1358 \; ; \; C_{RP1-H_2O_2} = 682.1)$

$$\mu_2 = \mu_1\frac{T_1 + C}{T_2 + C}\left(\frac{T_2}{T_1}\right)^{\frac{3}{2}} \tag{A.20}$$

The formulas required to determine the fluid flow parameters that are used in the thermal analysis. Reynolds and Prandtl expressions:

$$Re = \frac{\rho v D}{\mu} \qquad Pr = \frac{c_p\mu}{\kappa} \tag{A.21}$$

Adiabatic wall temperature T_{aw}, stagnation temperature T_0 and recovery factor R:

$$T_{aw} = R \cdot T_0 \tag{A.22}$$

$$T_0 = T\left(\frac{\gamma - 1}{2}ac\right) \tag{A.23}$$

$$R = \frac{1 + Pr^{1/3}(\frac{\gamma-1}{2})M^2}{1 + (\frac{\gamma-1}{2})M^2} \tag{A.24}$$

Maximum extracted heat from a coolant:

$$Q_{cooling,max} = \dot{m}_{coolant}\, c_{p,coolant}\, (T_{liquid,max} - T_0) \tag{A.25}$$

Appendix B

MMH & NTO figures

* Heat flux figures are not included ($\frac{J}{m^2s}$), instead showing section heat flux ($\frac{J}{ms}$).

B.1 Downscaled
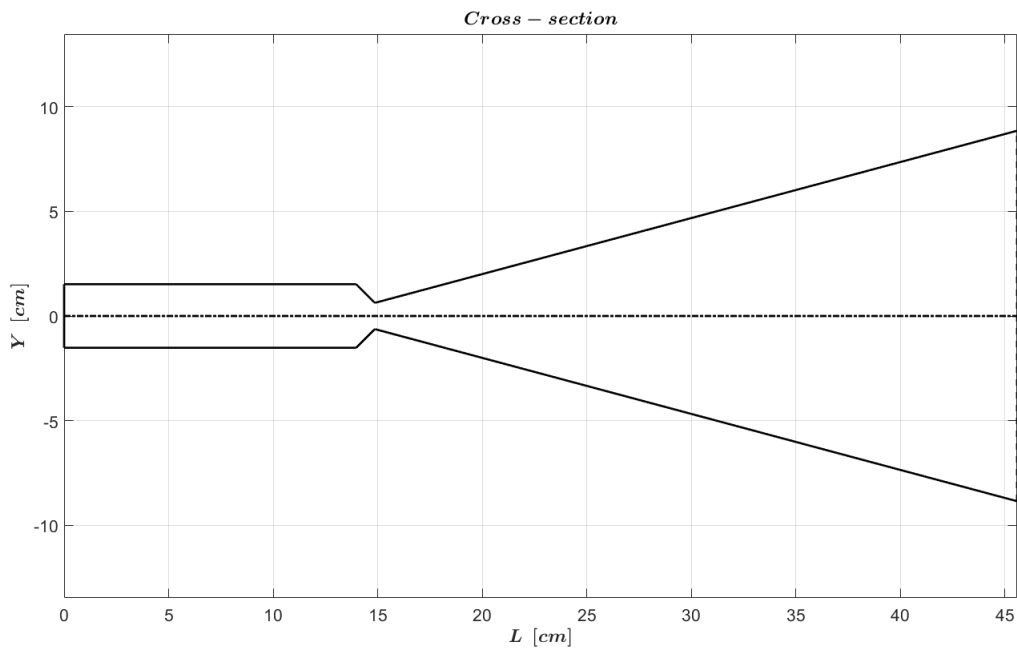
Figure B.1: Cross-section
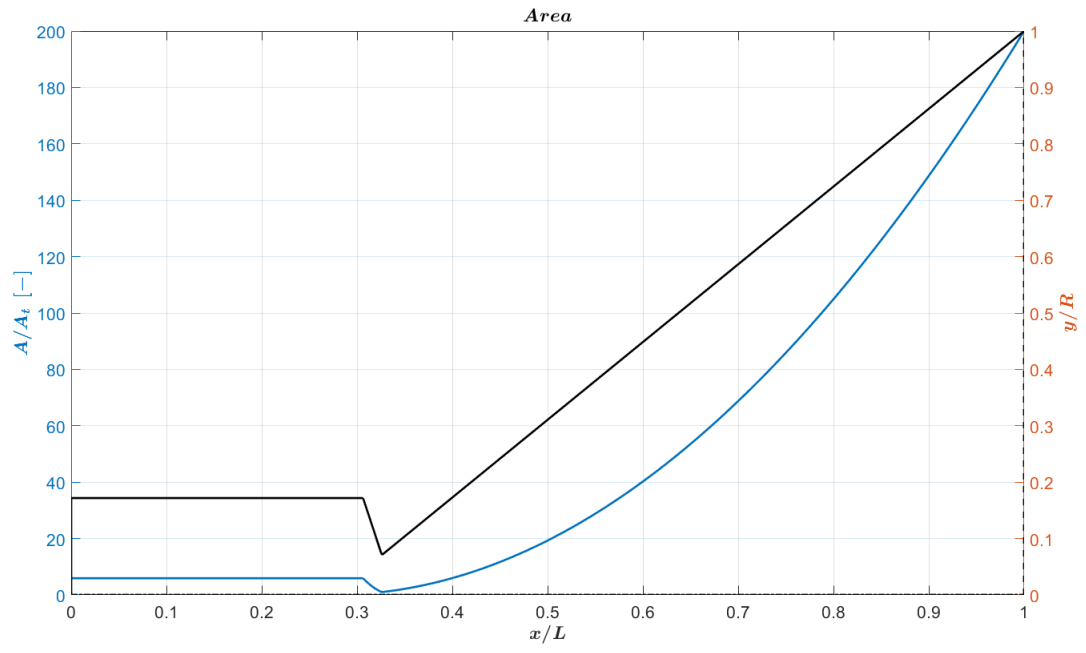
Figure B.2: Area vs position
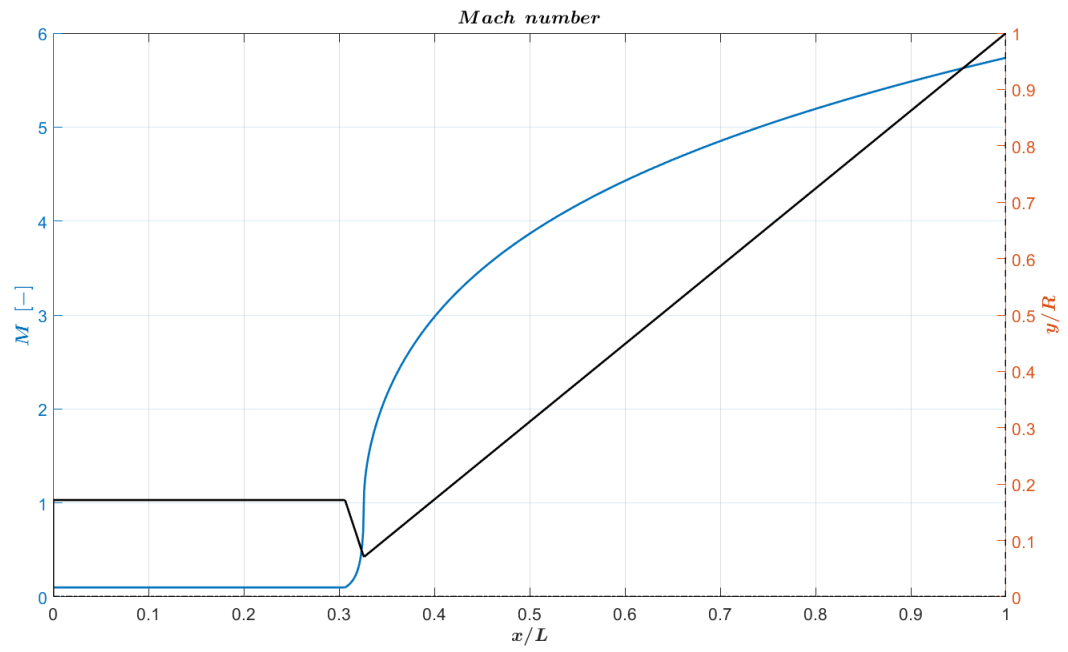
Figure B.3: Mach number
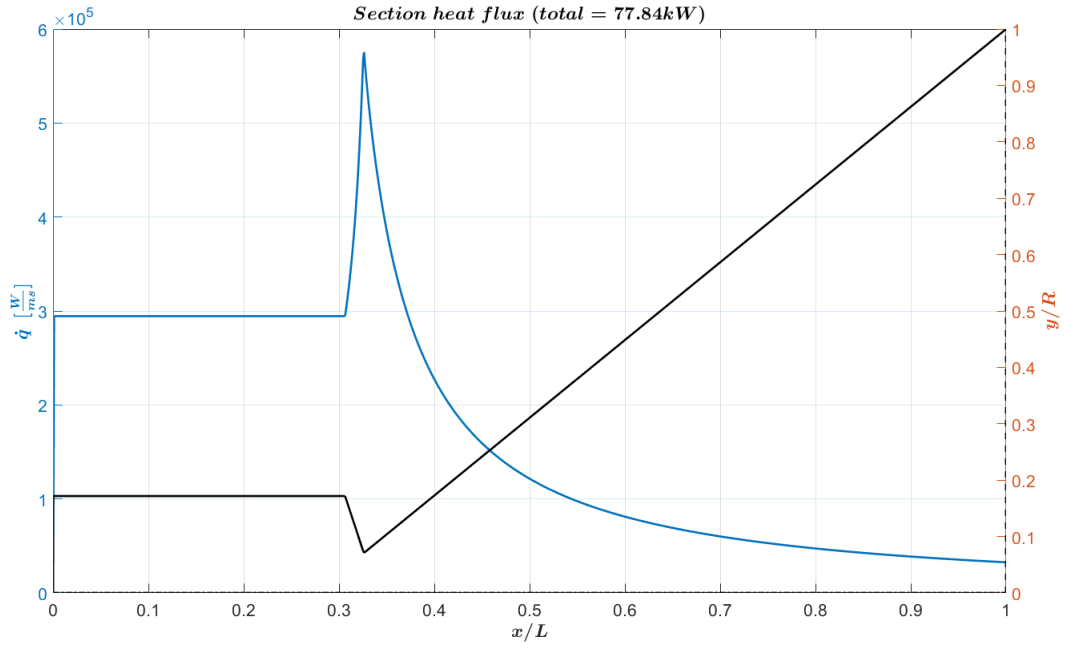
Figure B.4: Section heat flux
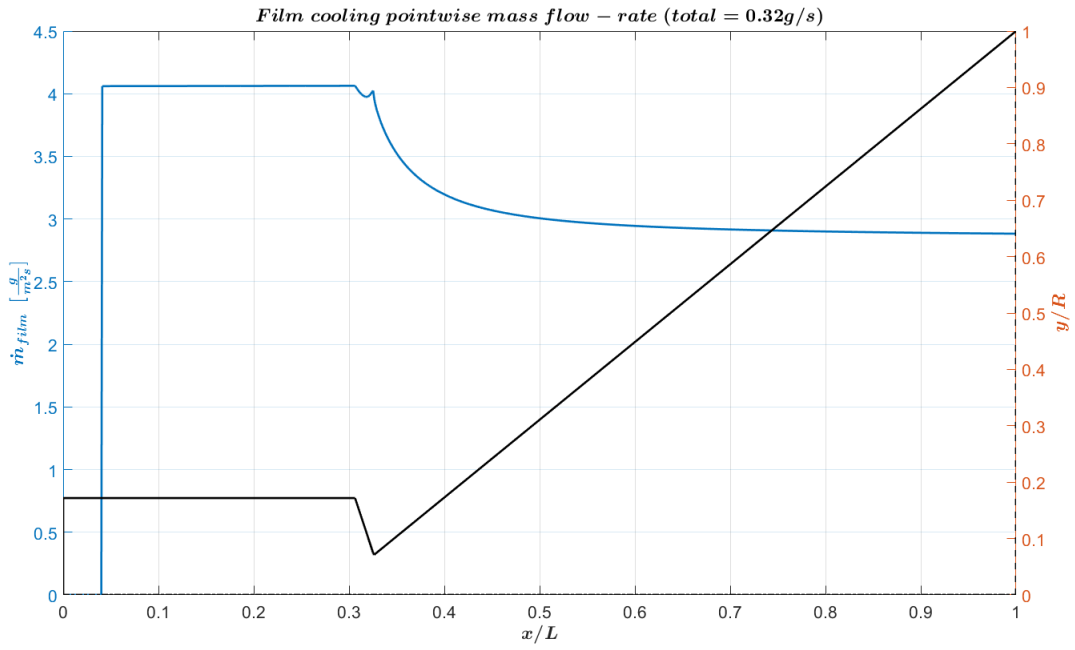
Figure B.5: Pointwise film flow rate
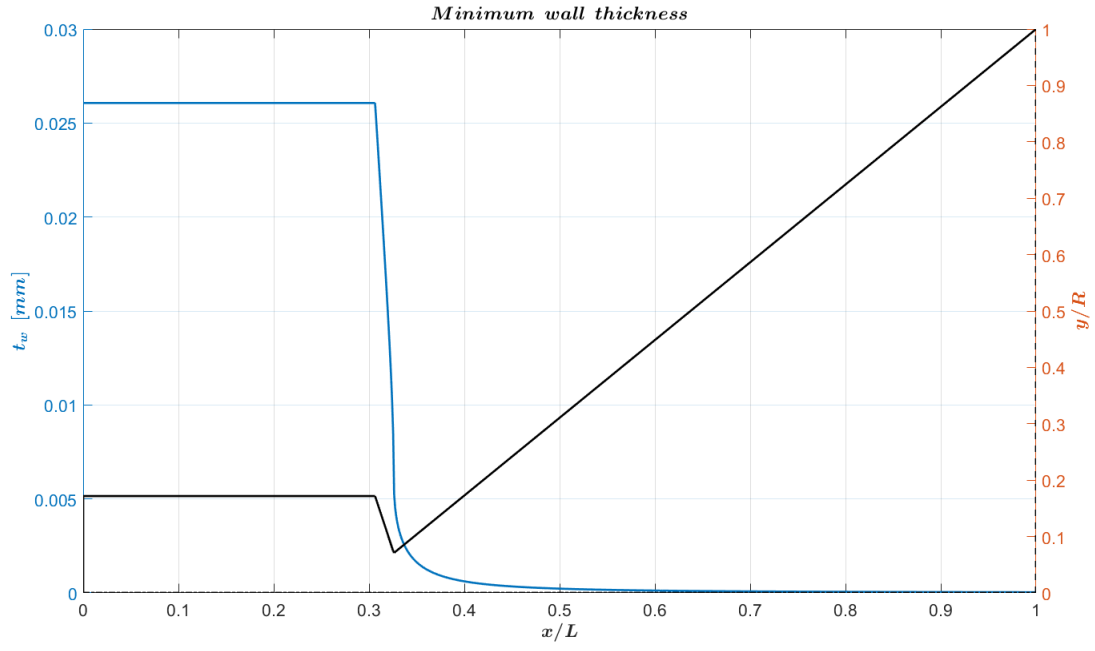
Figure B.6: Cylindrical pressure stress-derived minimum wall thickness

B.2 Nominal

* Including the ones showed throughout the report.
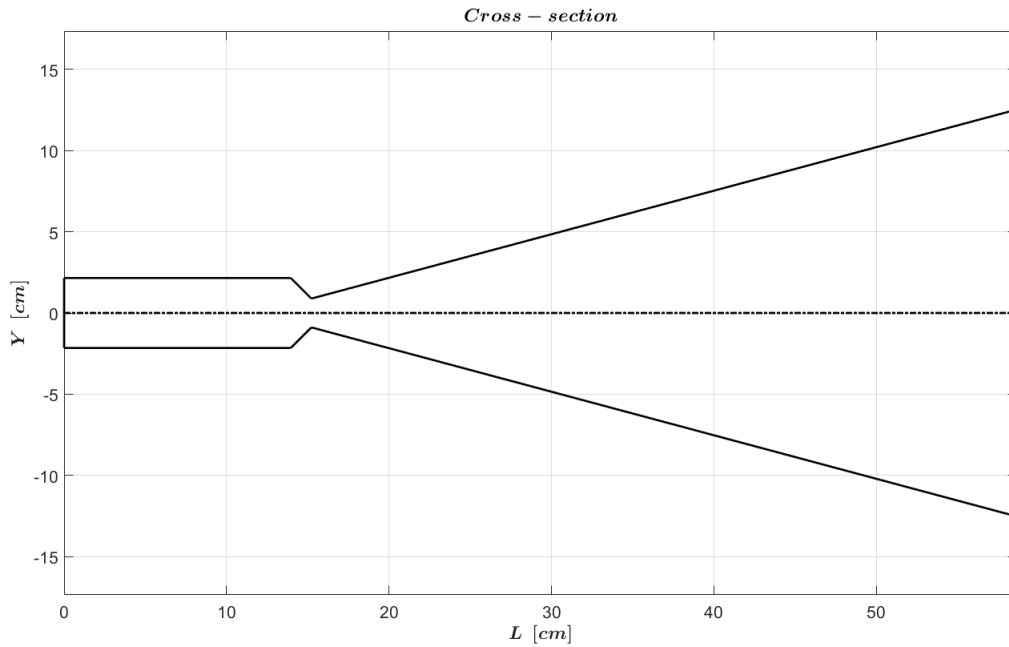
Figure B.7: Cross-section
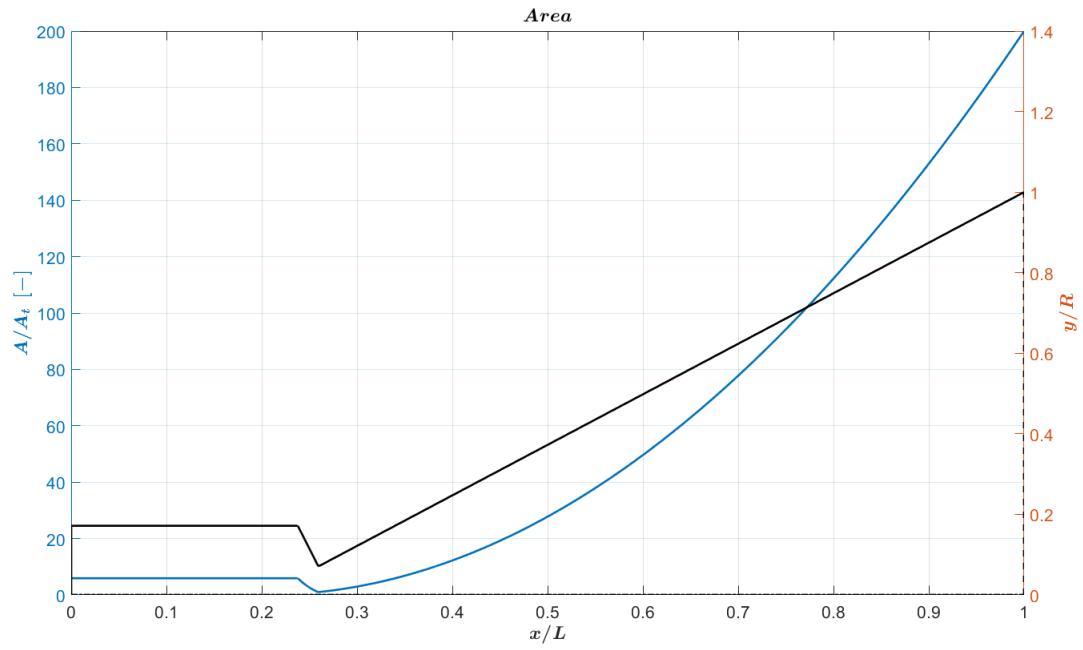
Figure B.8: Area vs position
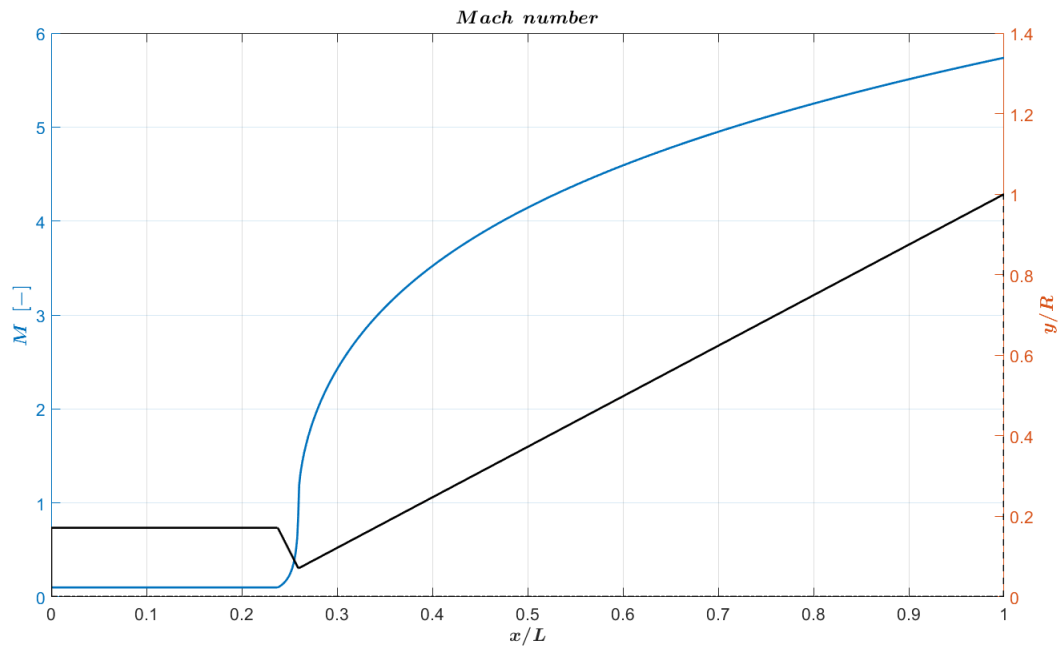
Figure B.9: Mach number
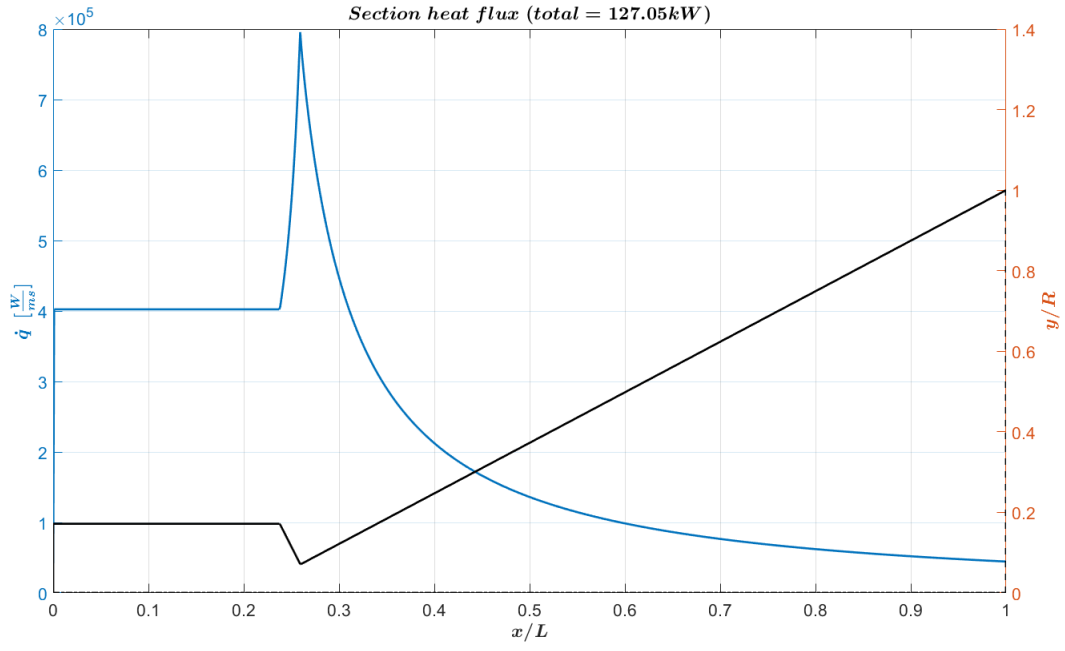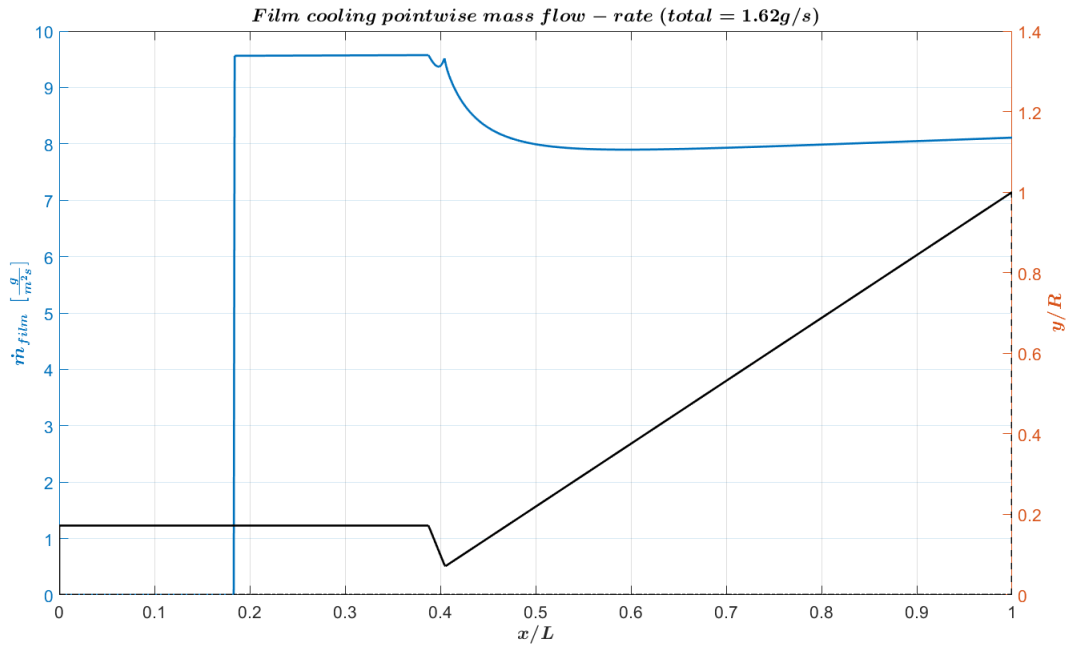
Figure B.10: Section heat flux
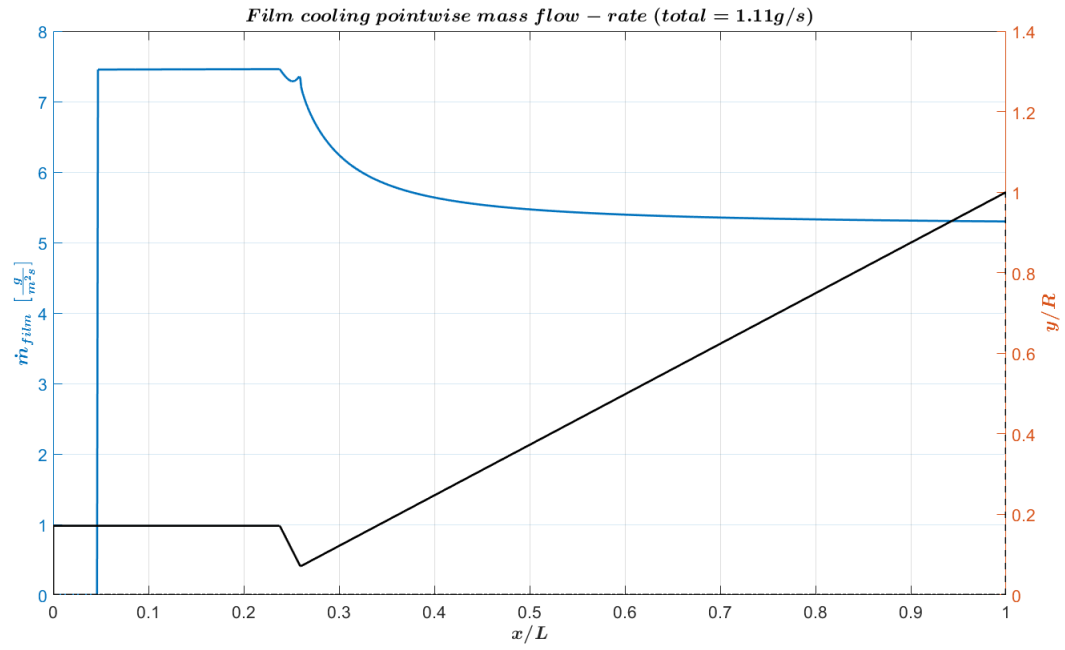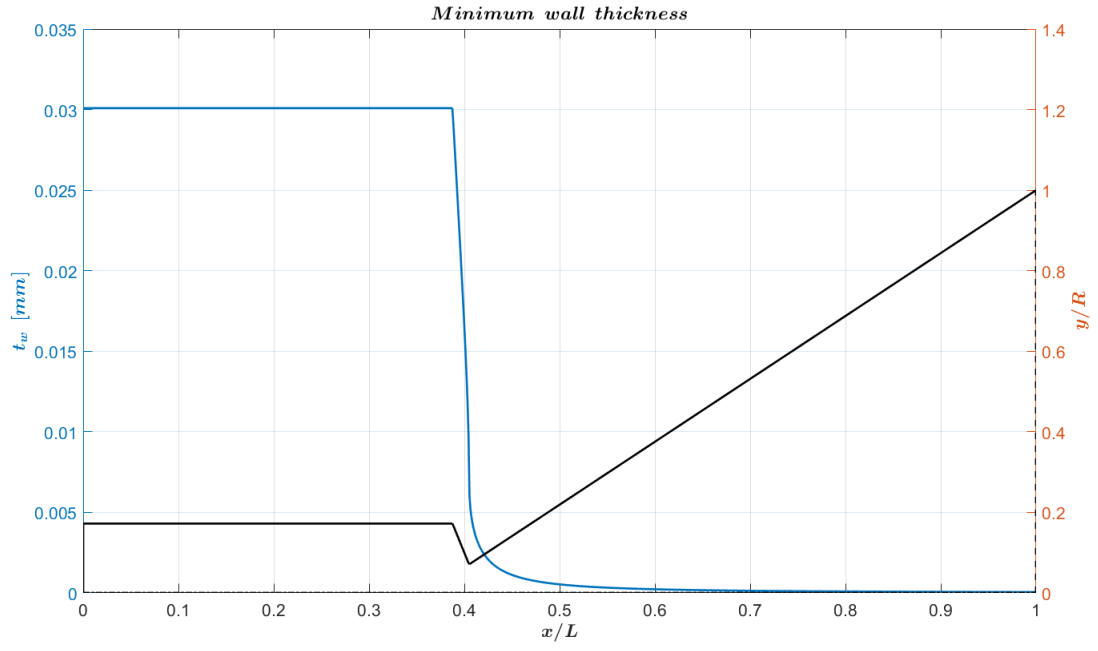

Figure B.11: Pointwise film flow rate
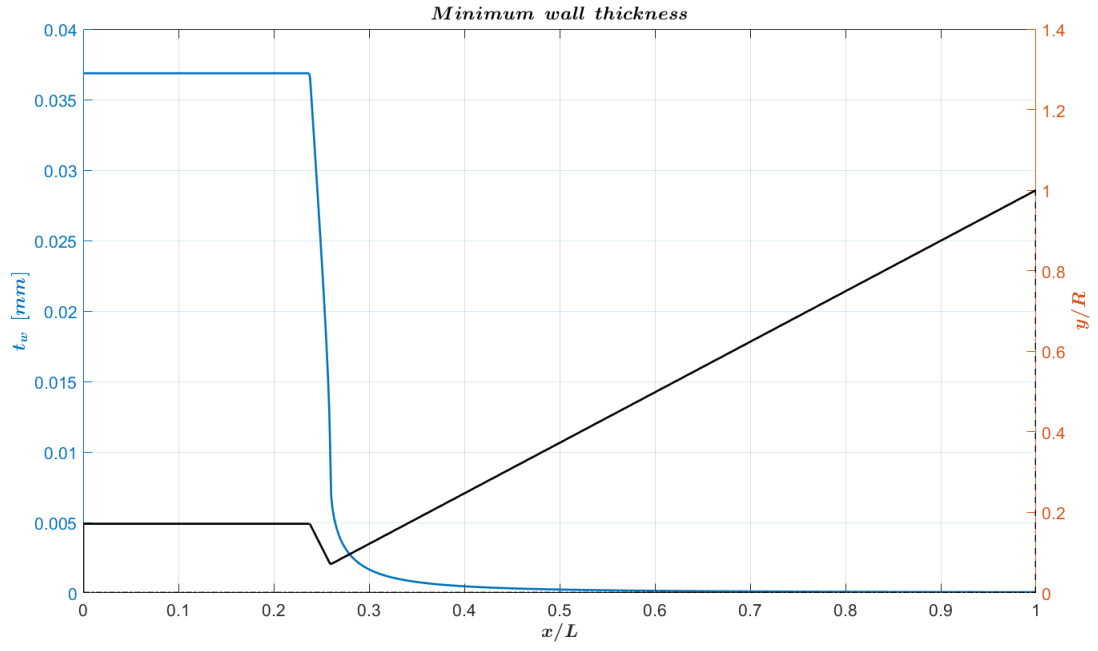
Figure B.12: Cylindrical pressure stress-derived minimum wall thickness
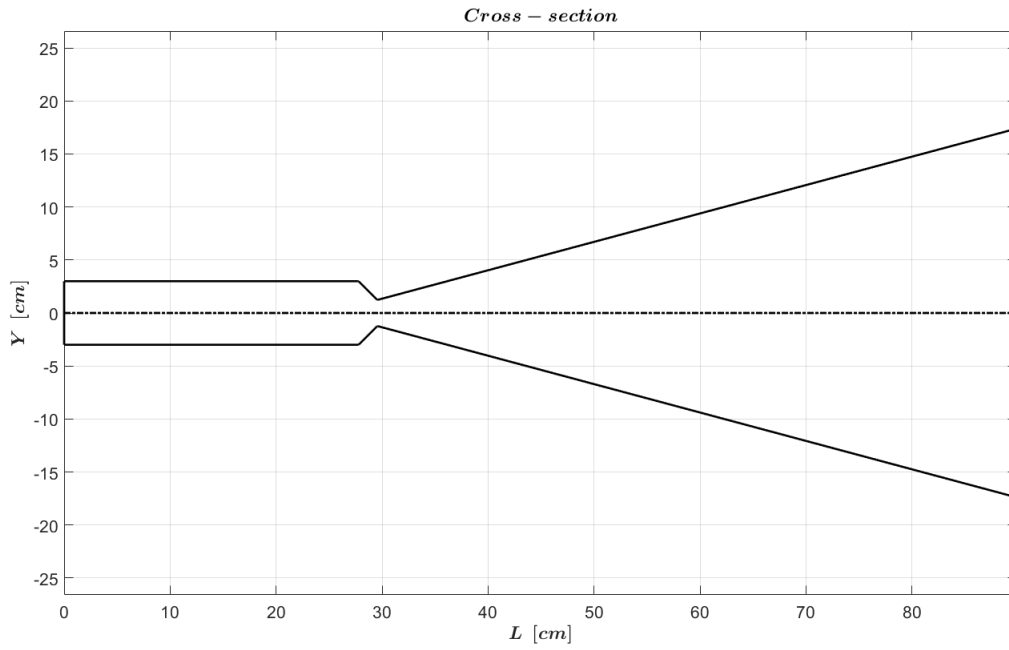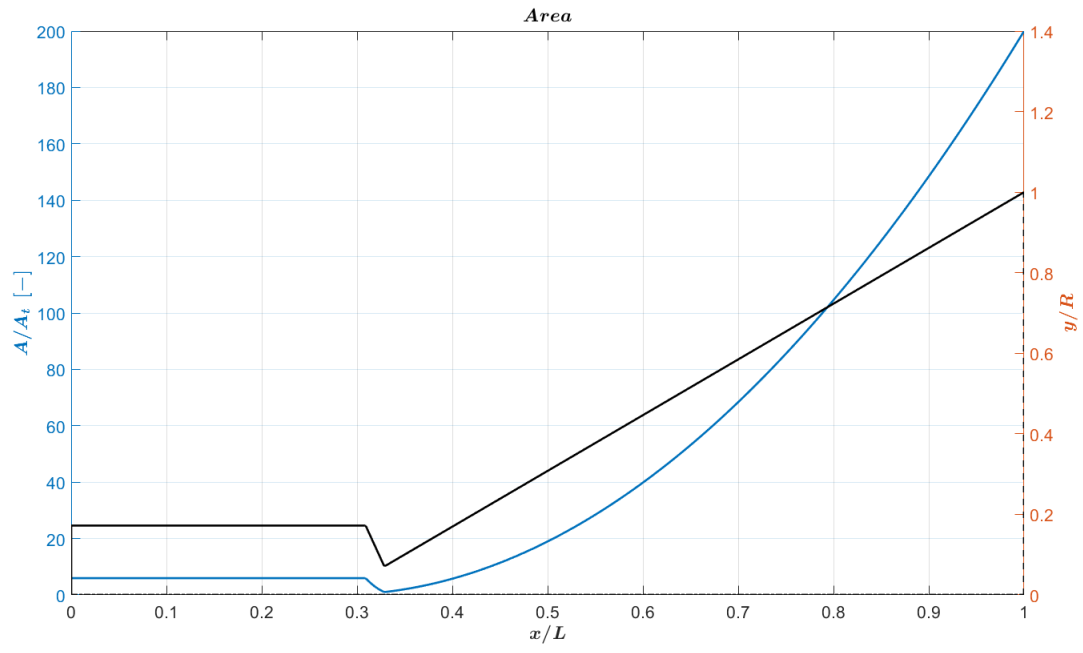
B.3   Upscaled
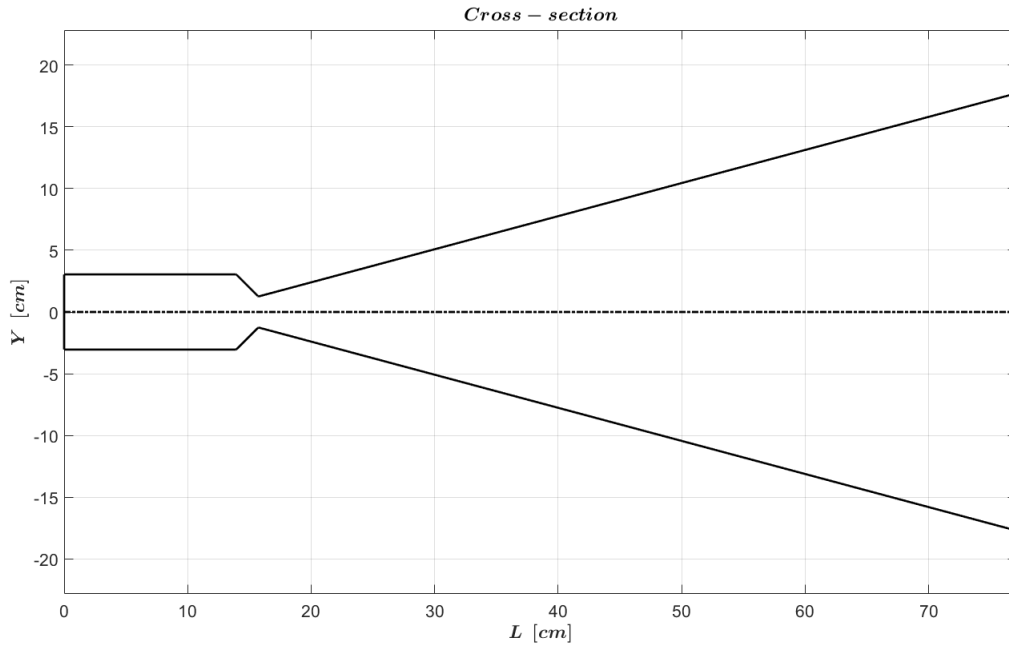
Figure B.13: Cross-section
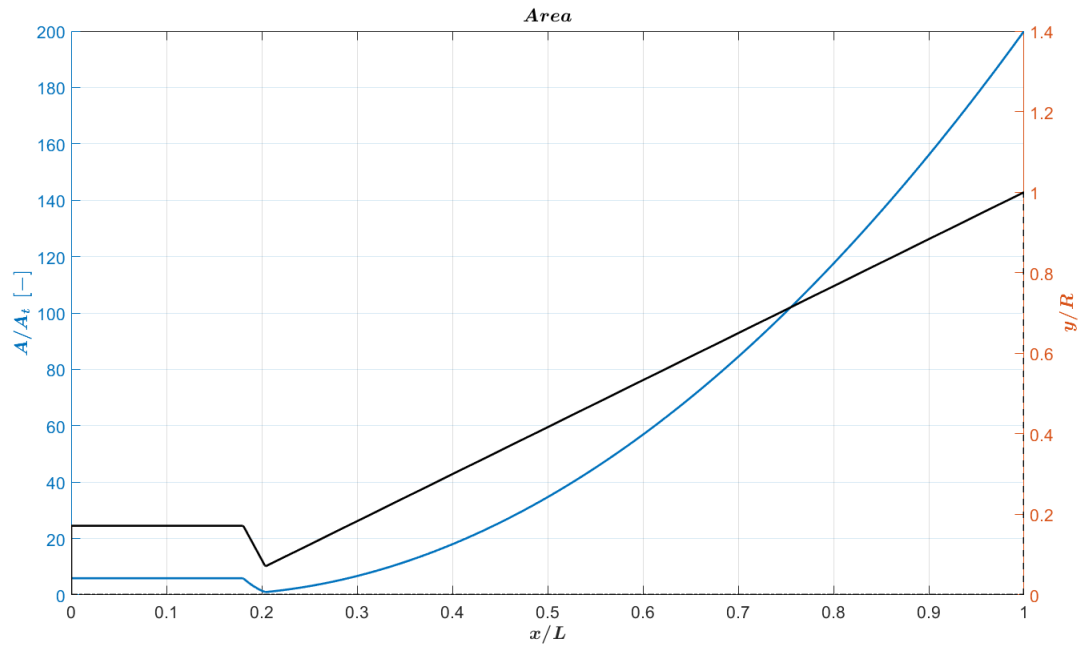
Figure B.14: Area vs position
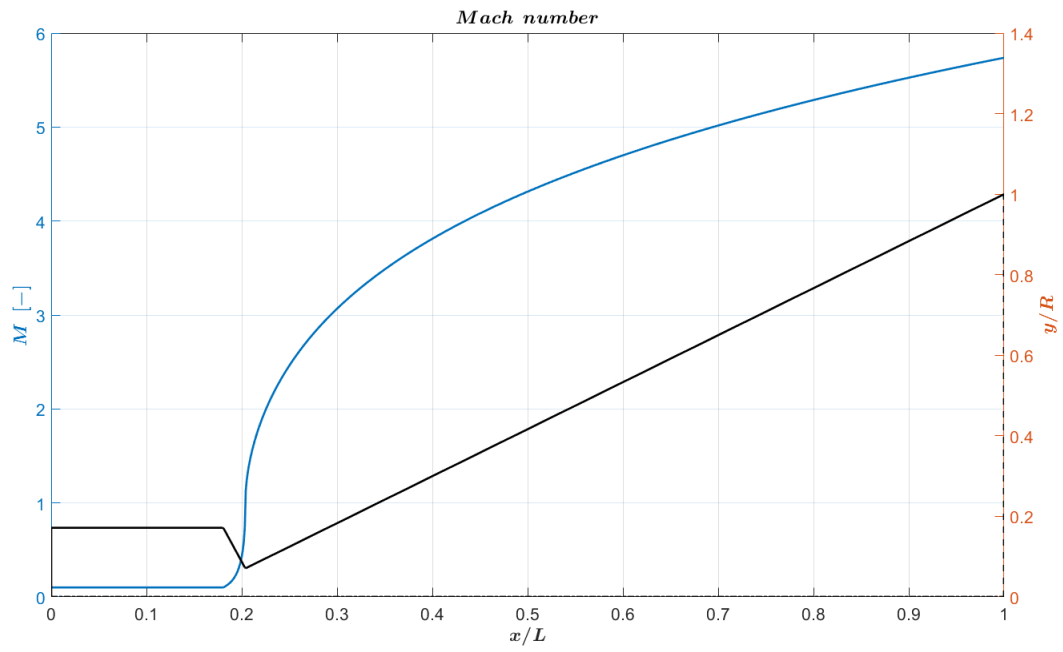
Figure B.15: Mach number
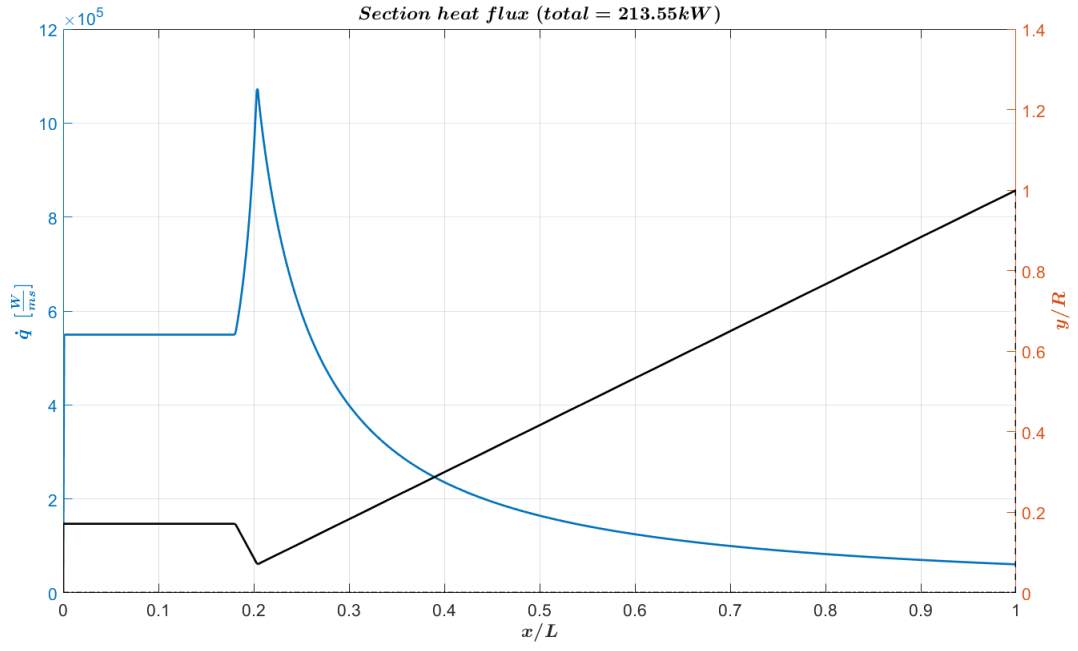
Figure B.16: Section heat flux
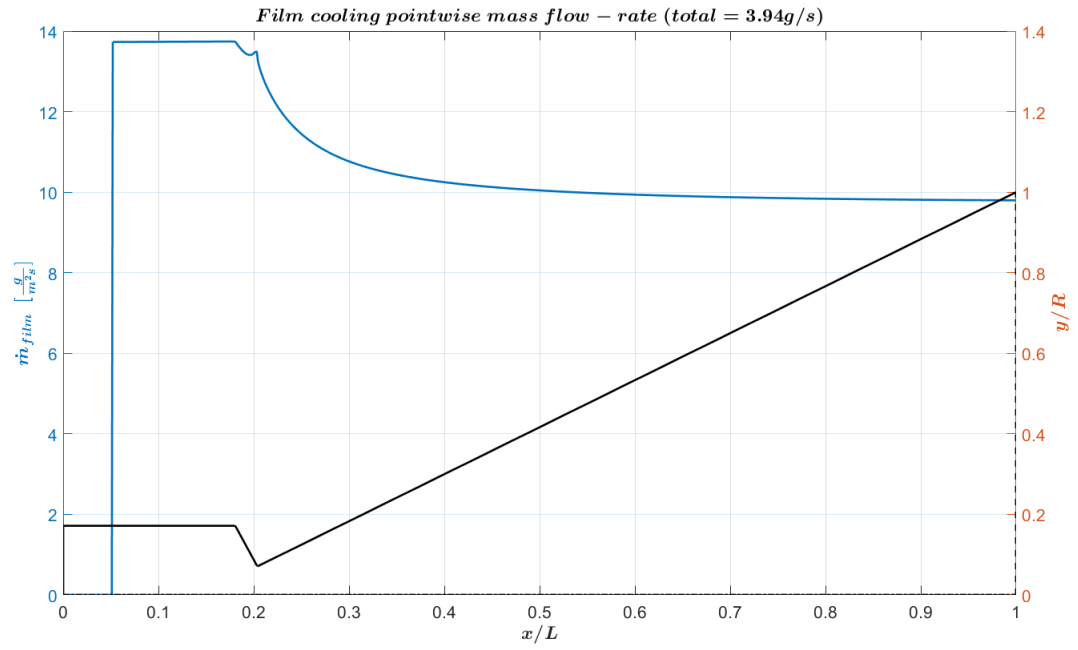
Figure B.17: Pointwise film flow rate
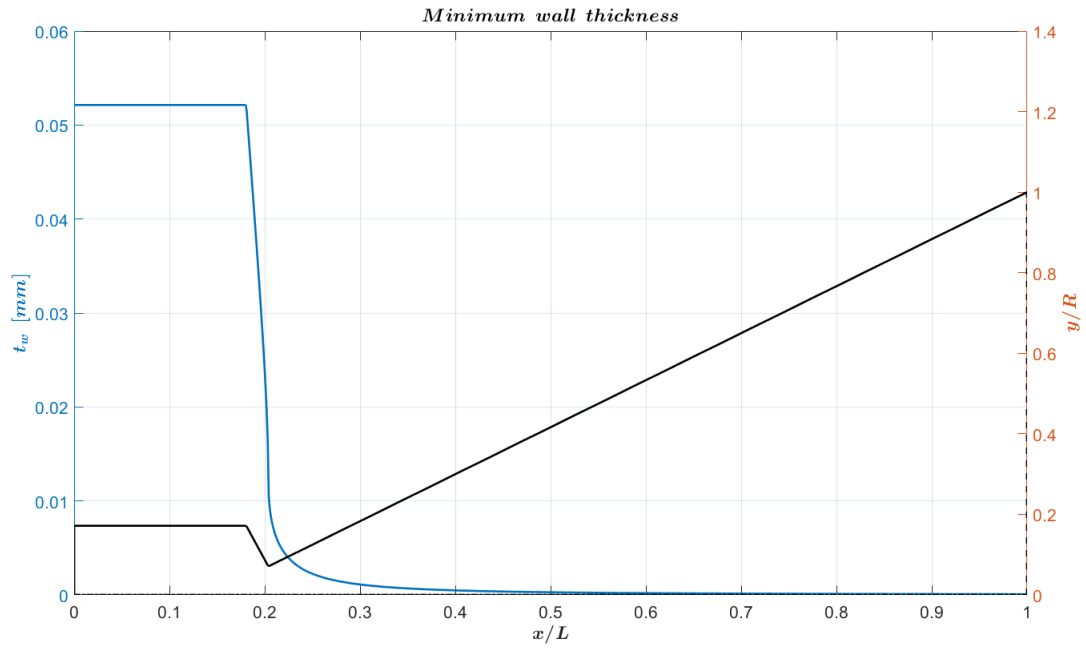
Figure B.18: Cylindrical pressure stress-derived minimum wall thickness

Appendix C

RP-1 & H_2O_2 figures

* Heat flux figures are not included $(\frac{J}{m^2 s})$, instead showing section heat flux $(\frac{J}{ms})$.

C.1 Downscaled
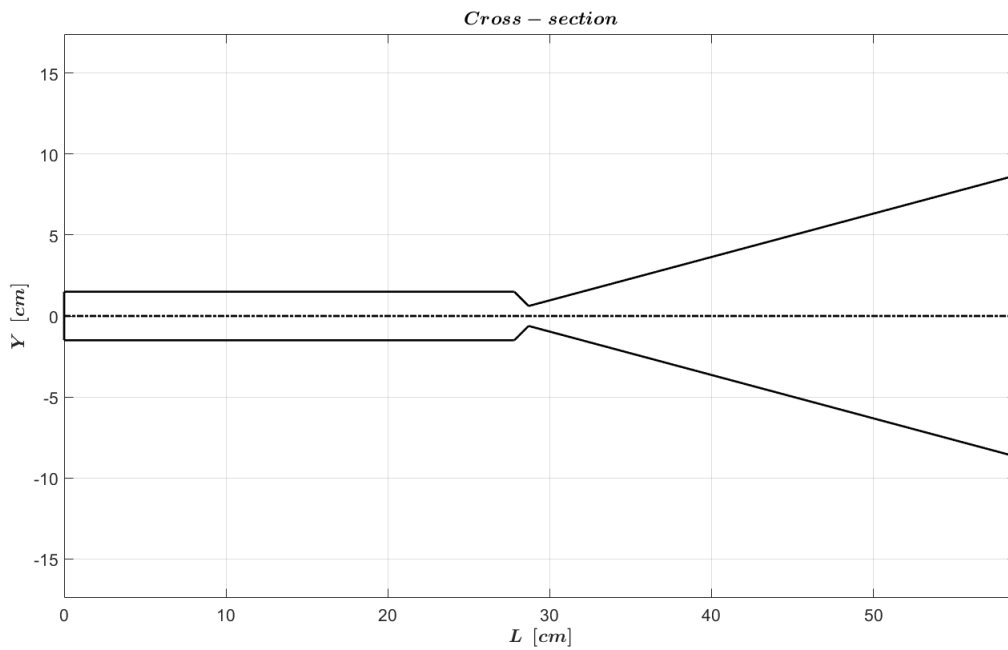
Figure C.1: Cross-section
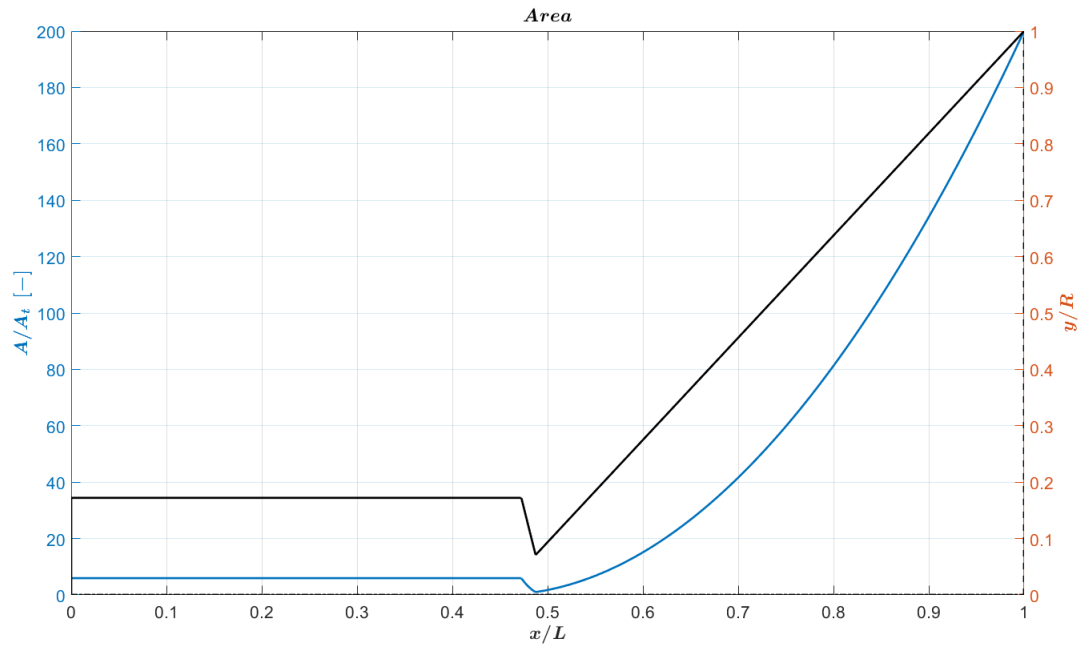
Figure C.2: Area vs position
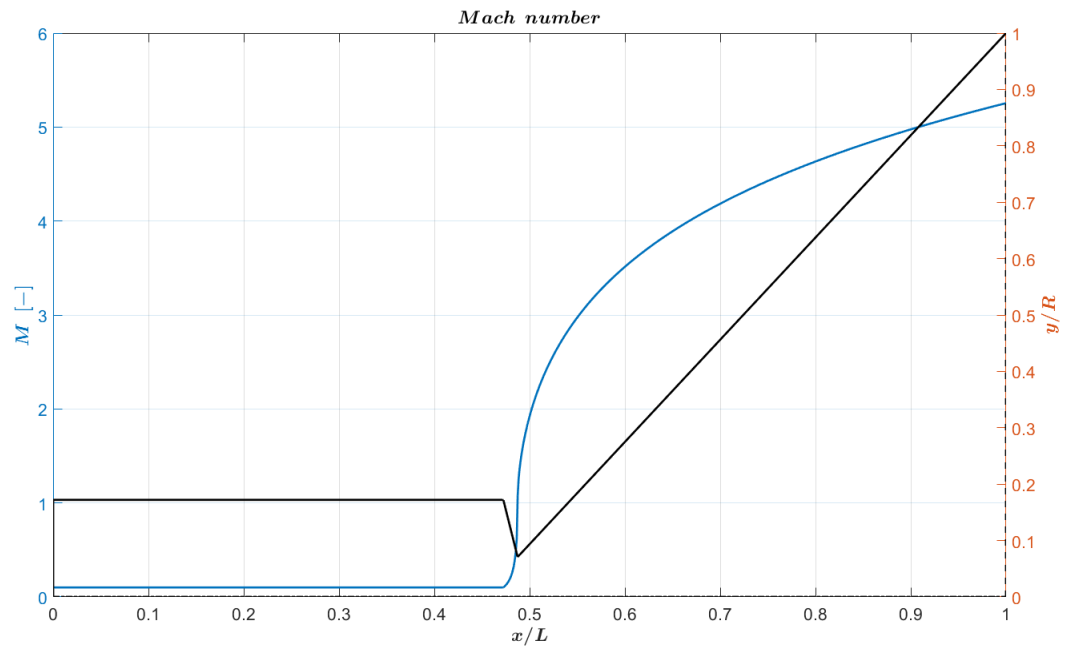
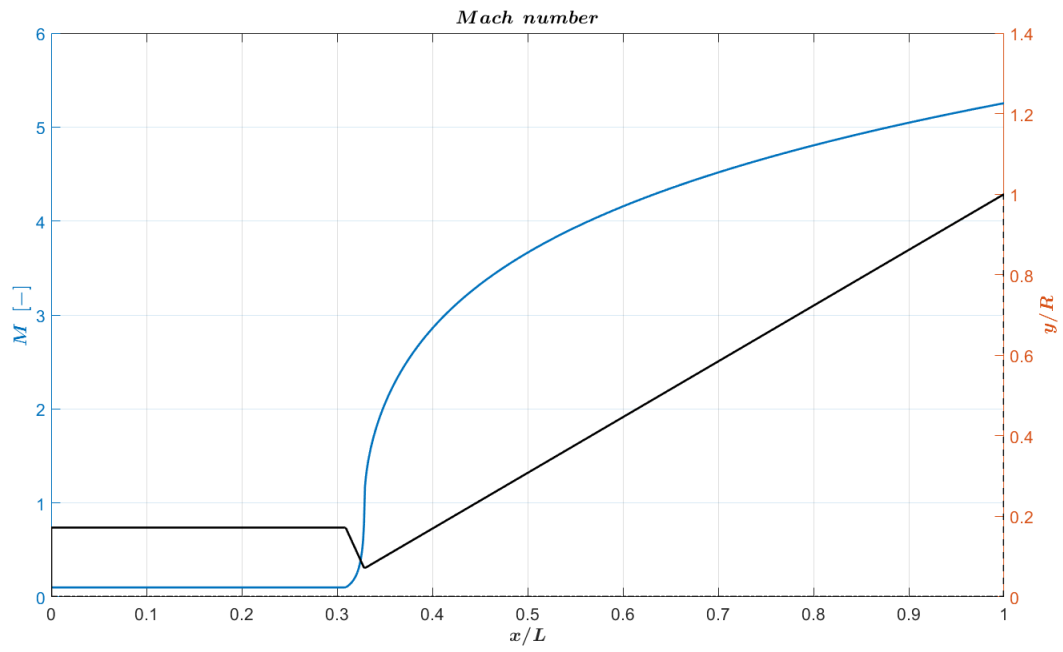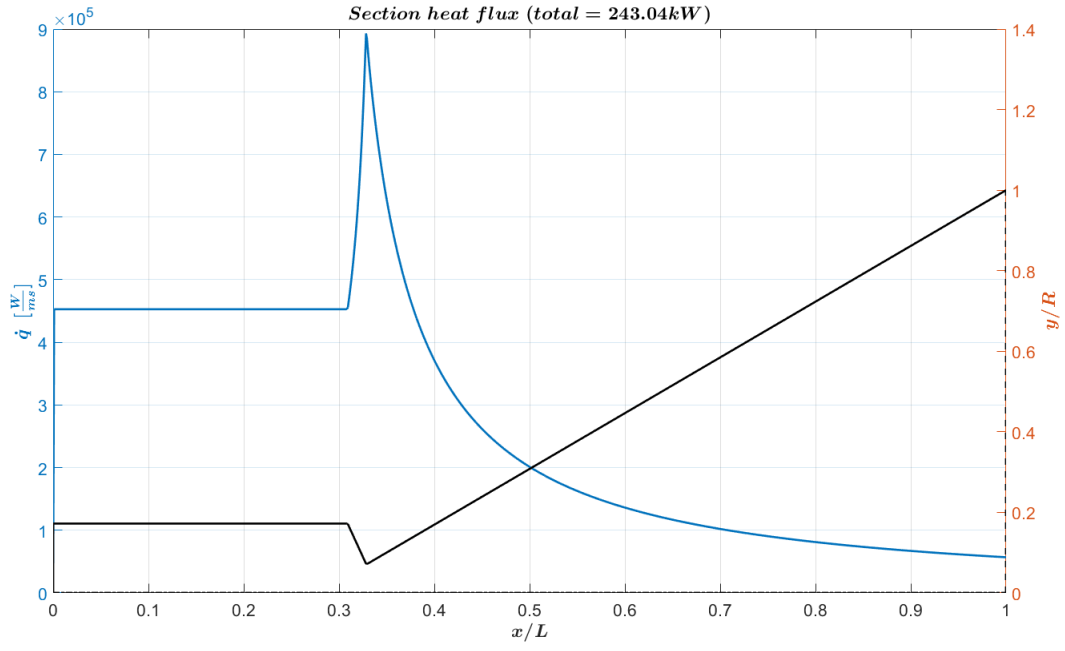
Figure C.3: Mach number
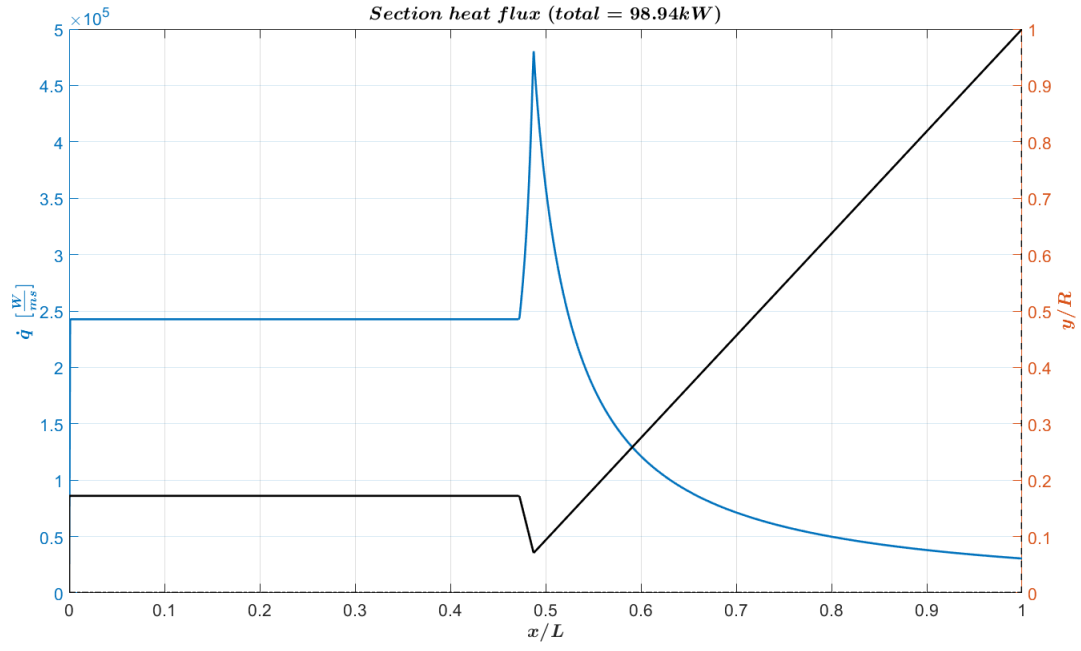
Figure C.4: Section heat flux
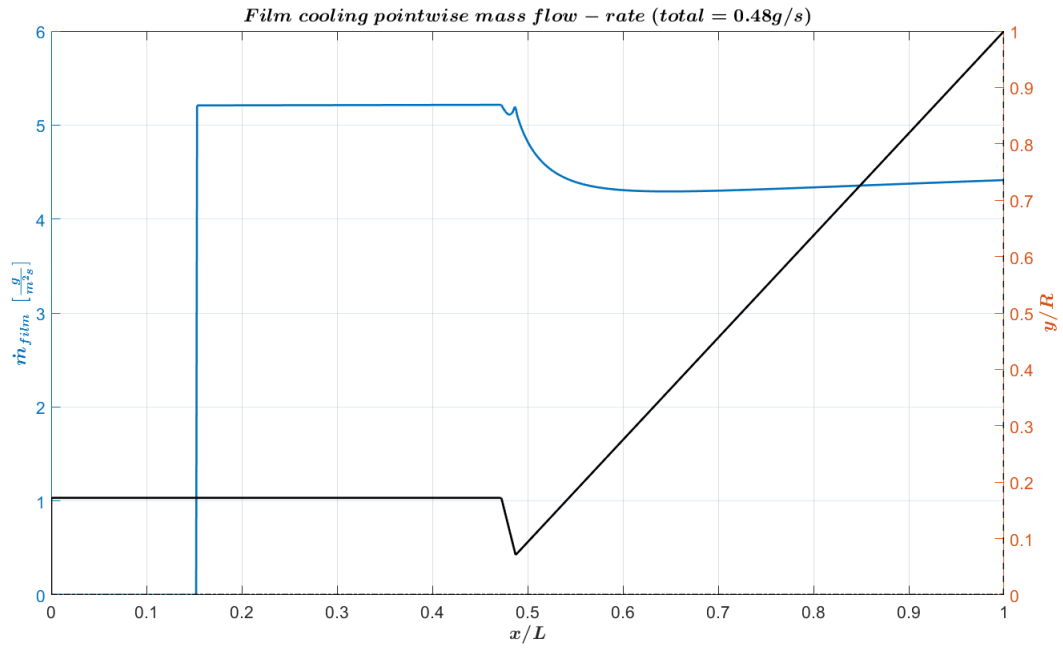
Figure C.5: Pointwise film flow rate

45
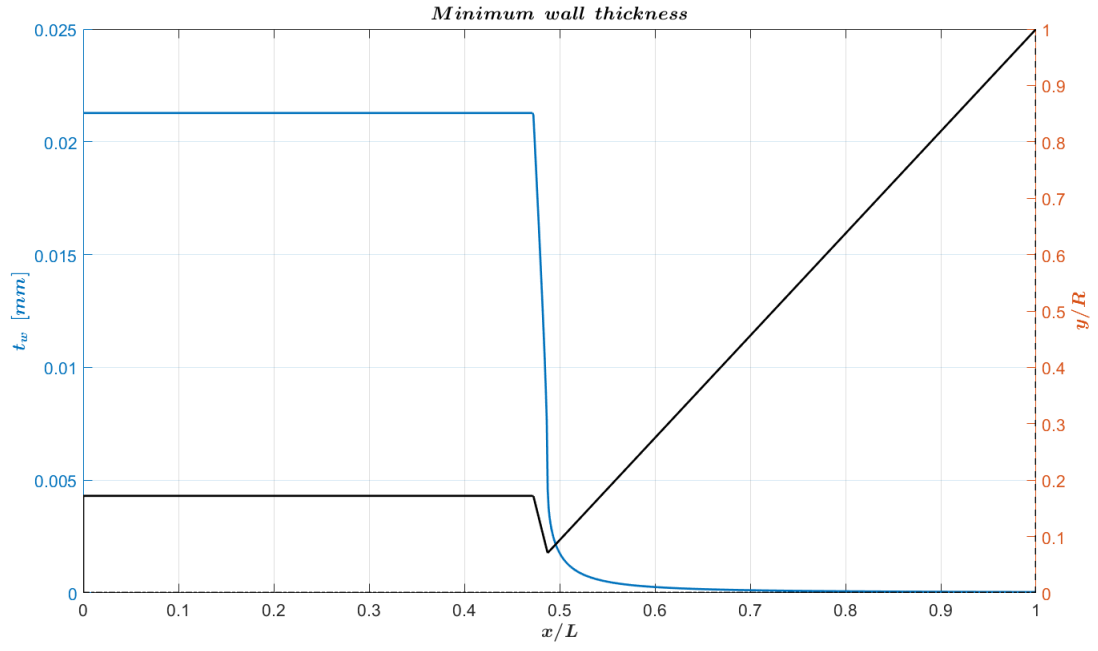
Figure C.6: Cylindrical pressure stress-derived minimum wall thickness

C.2 Nominal
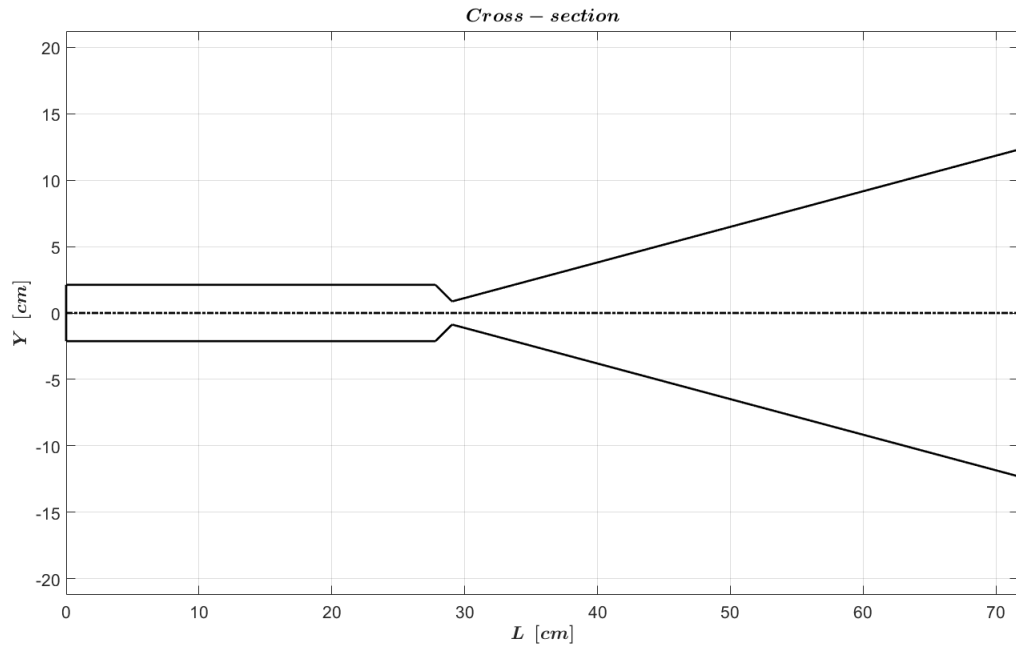
Figure C.7: Cross-section
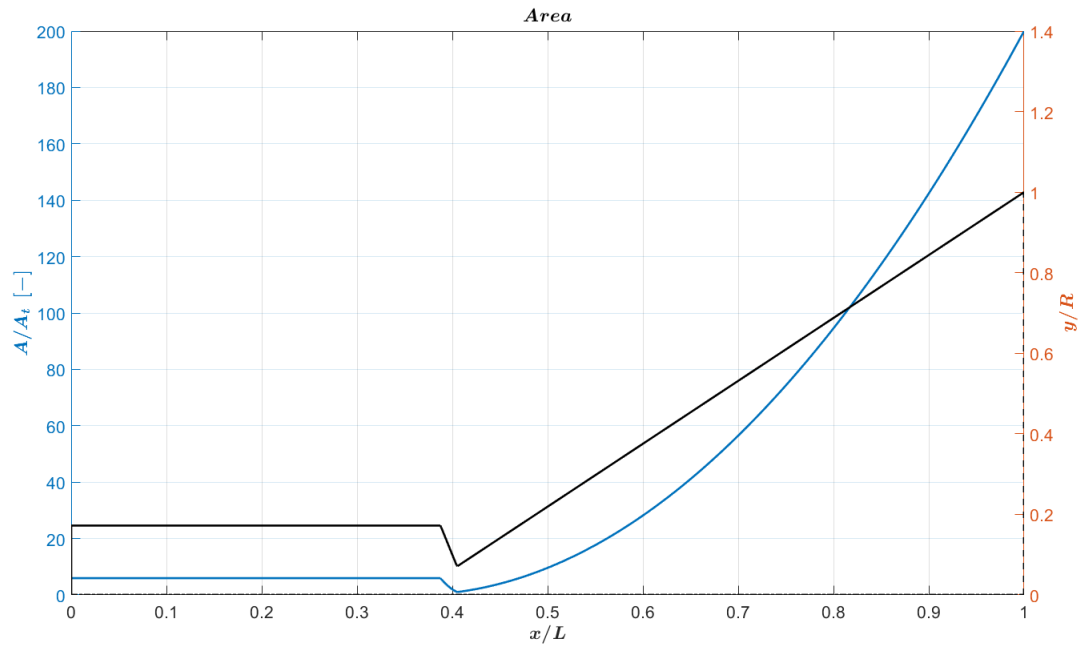
Figure C.8: Area vs position
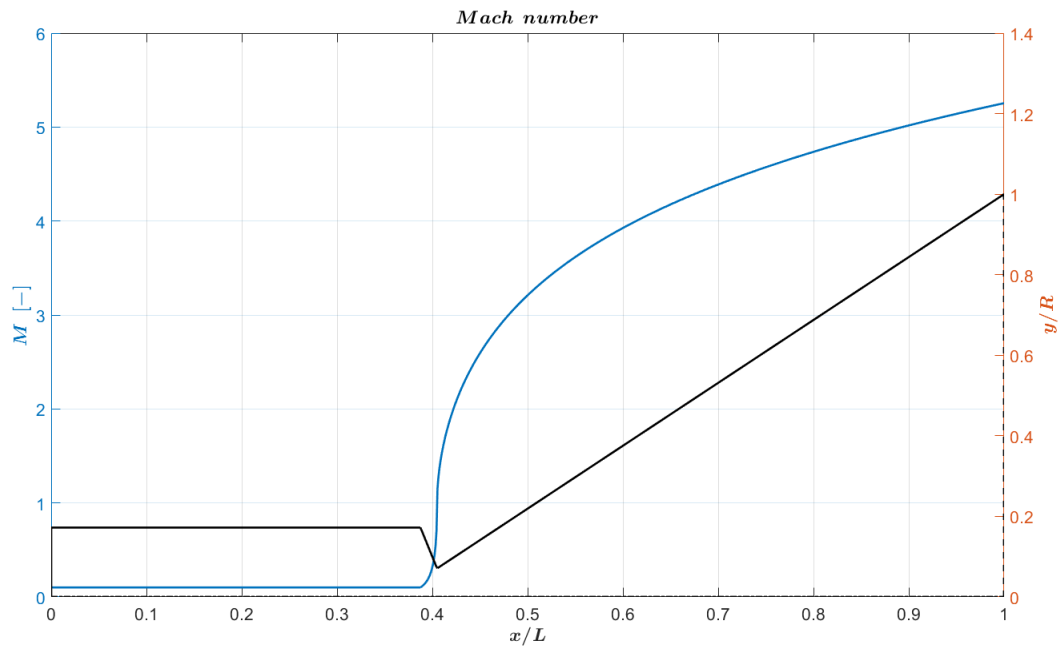
Figure C.9: Mach number
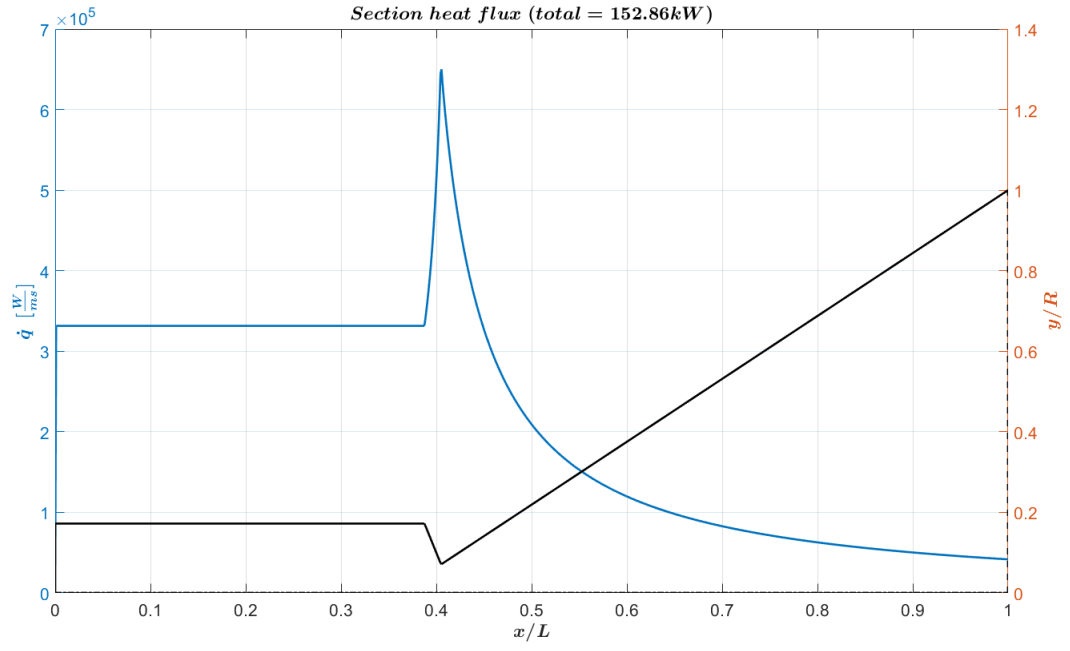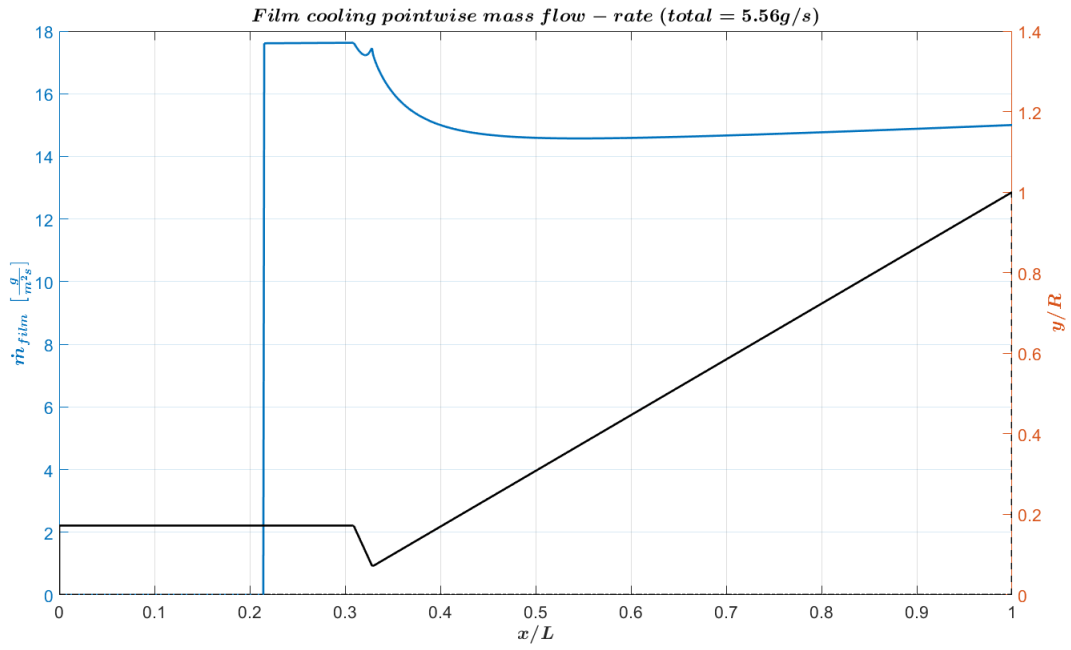
Figure C.10: Section heat flux

Figure C.11: Pointwise film flow rate

Figure C.12: Cylindrical pressure stress-derived minimum wall thickness

C.3 Upscaled

Figure C.13: Cross-section

Figure C.14: Area vs position

Figure C.15: Mach number

Figure C.16: Section heat flux
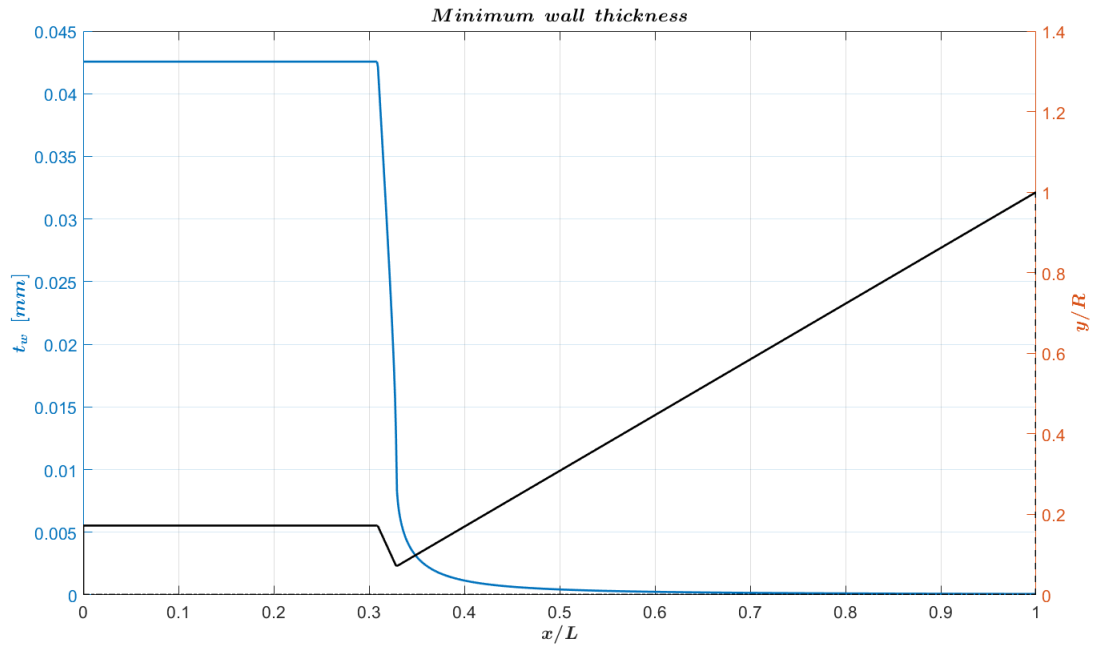

Figure C.17: Pointwise film flow rate

Figure C.18: Cylindrical pressure stress-derived minimum wall thickness